

Parsec-scale jet precession and a putative supermassive binary black hole system in the blazar AO 0235+164

F. B. da Silva Junior,^{1*} and A. Caproni,¹

¹Núcleo de Astrofísica, Universidade Cidade de São Paulo, R. Galvão Bueno 868, Liberdade, São Paulo, SP 01506-000, Brazil

Accepted 2025 July 17. Received 2025 June 23; in original form 2024 December 26

ABSTRACT

The blazar AO 0235+164 is a key source for studying the interplay between multi-wavelength variability in its light curves and changes in the position angles and apparent velocities of its parsec-scale jet components. In this work, we analyse public interferometric radio maps of AO 0235+164 at 15 and 43 GHz, using the Cross Entropy global optimisation technique to determine the structural parameters of its jet components. We identified 36 kinematically distinct jet components across all sky quadrants, indicating a highly relativistic parsec-scale jet with a minimum Lorentz factor of 34 ± 7 and a maximum viewing angle of $37^\circ \pm 8^\circ$. The temporal evolution of these jet components was modelled as a relativistic jet under a constant precession rate. The optimal clockwise precession model has a precession period of 8.4 ± 0.2 years, consistent with the 8.13-year periodicity previously detected in optical light curves, besides providing a time-variable Doppler boosting factor correlated with the most intense flares at gamma-ray energies. For the counter-clockwise precession, a period of 6.0 ± 0.1 years is found, compatible with the 5–6-year periodicities detected at radio and optical wavelengths. It is plausible that a supermassive black hole binary system in the nucleus of AO 0235+164 drives the parsec-scale jet precession and induces nodding motions consistent with short-term continuum periodicities. Nonetheless, alternative scenarios (e.g., intrinsic curved jet, warped accretion disc instabilities, Lense-Thirring/Bardeen-Petterson effects, dual jets) cannot be ruled out as causes or optional explanations for the precession.

Key words: black hole physics – techniques: interferometric – galaxies: active – BL Lacertae objects: individual: AO 0235 + 164 – galaxies: jets.

1 INTRODUCTION

Blazars are one of the most extreme types of active galactic nuclei (AGNs), with their jets forming a small angle relative to our line of sight (e.g., [Begelman et al. 1984](#); [Blandford et al. 2019](#)). It is commonly believed that such objects have a supermassive black hole (SMBH) surrounded by an accretion disk and/or optically thick plasma, a dusty torus, and a jet composed of multiple components usually moving at superluminal speeds (e.g., [Antonucci 1993](#); [Urry & Padovani 1995](#); [Netzer 2015](#)). Besides, these objects typically exhibit strong variability in their non-thermal continuum from radio to gamma-rays (e.g., [Urry & Padovani 1995](#); [Ulrich et al. 1997](#)).

Located at a redshift of 0.94 ([Cohen et al. 1987](#)), the blazar AO 0235+164 resides in a galaxy-rich field, potentially affected by gravitational lensing effects (e.g. [Stickel et al. 1988](#); [Abraham et al. 1993](#); [Webb et al. 2000](#)). AO 0235+164 exhibits strong variability across the entire electromagnetic spectrum (e.g. [Webb & Smith 1988](#); [Raiteri et al. 2008](#); [Rani et al. 2009](#); [Abdo et al. 2010](#)). Quasi-periodic radio variability has been reported in the literature, with periodicities around 1.8, 2.8, 3.7, 5.7, 10.0, 12.0 years ([Roy et al. 2000](#); [Raiteri et al. 2001](#); [Liu et al. 2006](#); [Fan et al. 2007b, 2016b](#); [Tripathi et al. 2021](#)). In the optical regime, periodicities of approximately 0.5, 1.3, 1.5, 2.8, 3.6, 5.8 and 8.2 years were also detected in the case of

AO 0235+164 (e.g. [Webb & Smith 1988](#); [Smith & Nair 1995](#); [Raiteri et al. 2001](#); [Fan et al. 2002](#); [Raiteri et al. 2006, 2008](#); [Wang 2014](#); [Fan et al. 2016a](#); [Fan et al. 2017](#); [Roy et al. 2022](#); [Otero-Santos et al. 2023](#)). Short-term variability, particularly at lower frequencies, may be caused by interstellar scintillation of ultra-compact components with a size of approximately $10 \mu\text{as}$ (e.g. [Rickett et al. 2006](#)).

Radio images of AO 0235+164 at kiloparsec scales show a "one-sided halo" morphology (e.g. [Cooper et al. 2007](#)), characterized by an extended structure on one side of an angularly unresolved nucleus that is surrounded by diffuse halo-like emission. AO 0235+164 is partially resolved in most radio bands when observed using Very Long Baseline Interferometry (VLBI) techniques. Previous VLBI studies of this source found a jet-like morphology at parsec scales (e.g. [Jones et al. 1984](#); [Chu et al. 1996](#); [Chen et al. 1999a](#); [Jorstad et al. 2001](#); [Kutkin et al. 2018](#)).

Association of flaring episodes with the emergence of superluminal jet components in AO 0235+164 was also reported in the literature (e.g. [Agudo et al. 2011](#); [Escudero Pedrosa et al. 2024](#)). The observed brightness temperature of the core region of AO 0235+164 is exceptionally high, reaching values as high as $10^{13.8}$ K ([Frey et al. 2000](#)), which exceeds the upper limit set by the Inverse Compton process (e.g., [Kellermann & Pauliny-Toth 1969](#)), even after considering extremely high Doppler boosting factors.

In this work, the study of public interferometric radio maps of AO 0235+164 obtained along almost the last 30 years has allowed the

* E-mail: flavio.junior94@cs.unicid.edu.br (KTS)

kinematic identification of 36 parsec-scale jet components moving relativistically from the core.

We show that changes in their position angles and apparent velocities over time are compatible with the precession of a relativistic jet with a period of approximately 8.4 years (or 6.0 years in the case of a counter-clockwise sense of precession). The feasibility of this jet precession being caused by a supermassive black hole binary system (SMBHB) is analysed, assuming that the orbital plane of the secondary supermassive black hole does not coincide with the primary accretion disc, which induces torques that cause the precession of the disc and the jet (e.g. Abraham 2000; Romero et al. 2000; Caproni & Abraham 2004a,b; Caproni et al. 2006, 2013).

This work is structured as follows: In section 2, it is provided a description of the interferometric radio data used in this work. The process of kinematic identification of the jet components in AO 0235+164, the estimates of lower limit for the jet bulk Lorentz factor, the upper limit for jet viewing angle, and the determination of the brightness temperature of the core region are presented in section 3. Temporal changes in the apparent velocity and position angle of the jet components are discussed in the context of the jet precession scenario in section 4. From the best of our knowledge, the variability of the brightness temperature of the core region is also included in the precession modellings for the first time in the literature. In section 5, we show that this jet precession may be related to the existence of a supermassive binary black hole system in AO 0235+164. The same putative binary scenario can also driven nodding motions, which are able to introduce additional (periodic) changes in the jet viewing angle, impacting the observed jet velocity and the jet position angle. Some of the short-term periodicities reported in the literature are also discussed in terms of this binary system in section 5. Alternative scenarios for jet precession or different mechanisms for driving jet precession in AO 0235+164 are presented in section 6. Final remarks are made in section 7.

Throughout this work, the Λ CDM cosmology is adopted with $H_0 = 71.0 \text{ km s}^{-1}$, $\Omega_M = 0.27$, $\Omega_\Lambda = 0.73$, which, for the redshift of AO 0235+164, leads to a luminosity distance $D_L = 6141.7 \text{ Mpc}$, and a linear scale of 7.91 pc mas^{-1} . It establishes a relationship between proper motion and linear velocity, resulting in $1.0 \text{ mas year}^{-1} = 50.07c$ for AO 0235+164, where c is the speed of light.

2 INTERFEROMETRIC DATA SET

In this work, we made use of interferometric images of AO 0235+164 obtained at 15 GHz and available on the site that hosts the MOJAVE project¹ (Monitoring Of Jets in Active galactic nuclei with VLBA Experiments; e.g. Lister et al. 2009). In the case of observations at 43 GHz, radio maps were downloaded from the public database hosted by the Blazar group at Boston University² (Jorstad et al. 2017; Weaver et al. 2022).

In total, we gathered 203 public FITS files containing 162 observations of AO 0235+164 at 43 GHz obtained between July 2007 and April 2023, and 41 radio maps at 15 GHz from July 1995 to March 2009. All these images had their original field of view narrowed with the aim to reduce the computational costs involved in the Cross-Entropy global optimisation technique used in their model fittings (e.g., Caproni et al. 2014).

¹ <https://www.cv.nrao.edu/MOJAVE/>

² <https://www.bu.edu/blazars/VLBAproject.html>

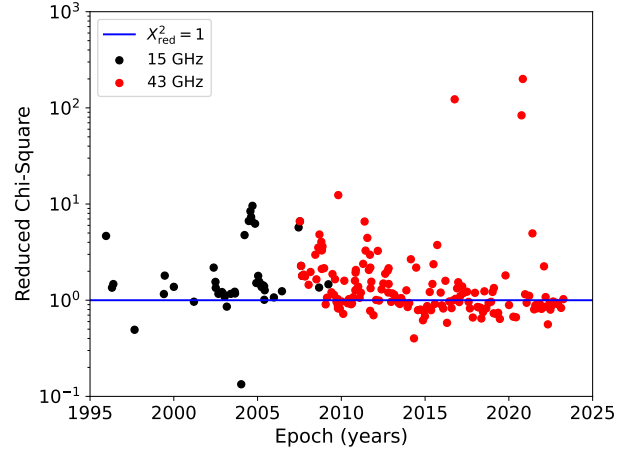


Figure 1. Reduced chi-squared values derived by fitting the complex visibility data of AO 0235+164 at 15 GHz (black circles) and 43 GHz (red circles) with elliptical Gaussian components, whose structural parameters were determined in the image plane via the CE optimisation technique. The blue horizontal line marks the unitary value for the reduced chi-square.

From the best of our knowledge, the incorporation of both interferometric data into the analyses conducted in this work makes our investigation about the kinematic behaviour of the parsec-scale jet of AO 0235+164 the most comprehensive from a temporal standpoint ever documented in the literature.

3 RESULTS

We assumed that the individual radio maps of AO 0235+164 can be decomposed into elliptical two-dimensional Gaussian components, where each of them depends on six independent parameters: peak intensity, I_0 , two-dimensional peak position (x_0, y_0) , with the coordinates x and y oriented respectively to right ascension and declination directions, semi-major axis, a , eccentricity, $\epsilon = \sqrt{1 - (b/a)^2}$, where b is the semi-minor axis, and the position angle of the major axis, ψ , measured positively from west to north.

The structural parameters of the Gaussian components were determined using our Cross-Entropy (CE) global optimisation method (e.g., Rubinstein 1997; Caproni et al. 2009), already applied to other blazars in the context of interferometric radio images (Caproni et al. 2014, 2017; Sumida et al. 2021; Nandi et al. 2024). Following the criteria proposed by Caproni et al. (2014), we determined the optimal number of Gaussian components in each one of the 203 images of AO 0235+164 analysed in this work. Those procedures detected a single component (core) in a few epochs, not exceeding five simultaneous Gaussian components (core plus four jet components) during the approximately 28 years of monitoring covered in this work.

To assess the reliability of those elliptical Gaussian components in the uv -plane, we retrieved the corresponding calibrated complex visibility data of AO 0235+164 from the public archives of the MOJAVE project and the Blazar Group at Boston University. These uv -data were modelled using the task MODELFIT in the DIFMAP software package (Shepherd et al. 1994) after feeding it with the CE-optimised values of the structural parameters of the Gaussian components. This allowed us to compute the reduced chi-squared values of the fits directly in the visibility domain, which are shown in Figure 1. The

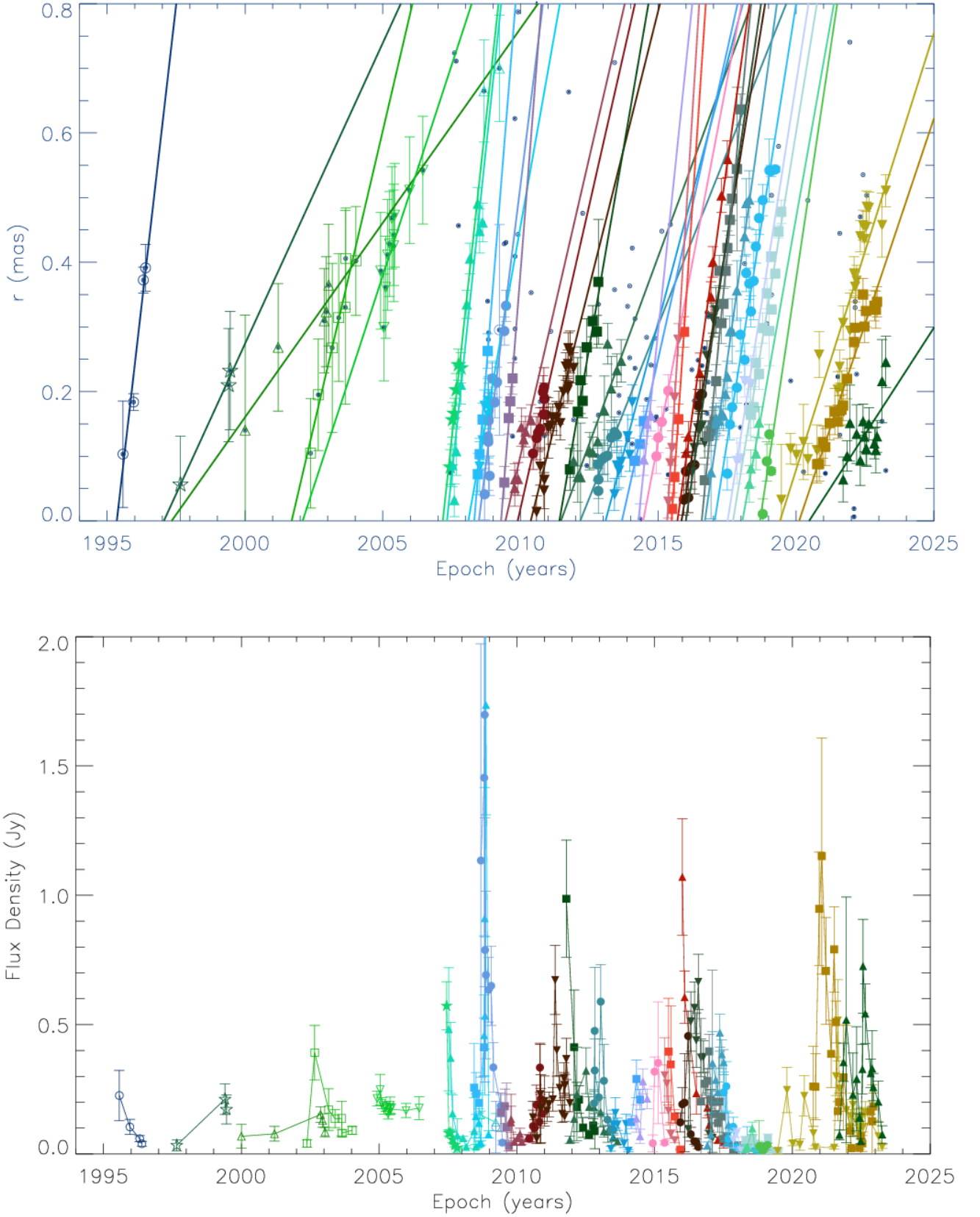


Figure 2. *Top panel:* Time evolution of the core-component distance of the 36 jet components of AO 0235+164 identified in this work. Open symbols represent jet components identified at 15 GHz, while filled symbols correspond to those at 43 GHz. Straight lines represent the linear regression for each individual component, while gray points are unidentified jet components from the kinematic point of view. *Bottom panel:* Flux density behaviour of the same 36 jet components.

Table 1. Kinematic parameters of the CE model-fitting jet components of AO 0235+164 identified in this work.

Jet component	t_0 (yr)	μ ($\mu\text{as yr}^{-1}$)	β_{app}	$\bar{\eta}$ (deg)	$N_{\text{epoch}}^{\text{a}}$	r_{p}
C1	1995.35 \pm 0.12	370.8 \pm 57.3	18.6 \pm 2.9	-20.6 \pm 7.6	4	0.980
C2	1997.06 \pm 0.54	93.0 \pm 25.6	4.7 \pm 1.3	-37.6 \pm 3.8	3	0.996
C3	1997.34 \pm 1.10	60.2 \pm 13.7	3.0 \pm 0.7	-73.2 \pm 4.1	5	0.949
C4	2001.69 \pm 0.24	182.4 \pm 26.0	9.1 \pm 1.3	-77.3 \pm 2.9	7	0.970
C5	2002.09 \pm 0.68	130.3 \pm 26.5	6.5 \pm 1.3	-29.6 \pm 0.5	11	0.846
C6	2007.18 \pm 0.14	395.8 \pm 117.5	19.8 \pm 5.9	-255.2 \pm 0.6	7	0.945
C7	2007.33 \pm 0.05	406.4 \pm 21.9	20.3 \pm 1.1	-24.7 \pm 4.0	11	0.961
C8	2008.10 \pm 0.27	240.7 \pm 94.1	12.1 \pm 4.7	-210.0 \pm 4.9	8	0.882
C9	2008.32 \pm 0.08	534.2 \pm 137.2	26.7 \pm 6.9	-167.4 \pm 1.7	4	0.999
C10	2008.49 \pm 0.08	344.3 \pm 45.9	17.2 \pm 2.3	-201.9 \pm 18.1	11	0.931
C11	2009.29 \pm 0.10	545.9 \pm 170.7	27.3 \pm 8.5	-198.1 \pm 0.4	4	0.994
C12	2009.45 \pm 0.23	184.6 \pm 70.0	9.2 \pm 3.5	-224.8 \pm 1.8	7	0.898
C13	2009.89 \pm 0.39	187.9 \pm 84.2	9.4 \pm 4.2	-205.2 \pm 0.8	9	0.849
C14	2010.37 \pm 0.14	170.5 \pm 21.8	8.5 \pm 1.1	-200.4 \pm 3.8	18	0.943
C15	2011.41 \pm 0.16	247.3 \pm 39.3	12.4 \pm 2.0	-193.6 \pm 6.4	8	0.962
C16	2011.46 \pm 0.25	115.7 \pm 20.1	5.8 \pm 1.0	-182.8 \pm 3.3	11	0.906
C17	2012.16 \pm 0.45	106.9 \pm 50.0	5.4 \pm 2.5	-76.2 \pm 9.1	9	0.910
C18	2013.08 \pm 0.26	160.5 \pm 61.5	8.0 \pm 3.1	-110.7 \pm 7.9	7	0.878
C19	2013.68 \pm 0.57	190.5 \pm 164.7	9.5 \pm 8.2	-60.7 \pm 1.2	3	0.982
C20	2014.28 \pm 0.09	409.3 \pm 129.7	20.5 \pm 6.5	-68.2 \pm 2.6	4	0.931
C21	2014.45 \pm 0.34	223.8 \pm 113.2	11.2 \pm 5.7	-34.9 \pm 0.6	4	0.990
C22	2015.32 \pm 0.05	686.0 \pm 132.0	34.3 \pm 6.6	-50.4 \pm 0.5	5	0.996
C23	2015.48 \pm 0.05	642.3 \pm 114.8	32.2 \pm 5.7	-113.1 \pm 3.0	4	1.000
C24	2015.69 \pm 0.10	305.9 \pm 26.3	15.3 \pm 1.3	-302.6 \pm 0.7	7	0.996
C25	2015.84 \pm 0.11	263.5 \pm 58.1	13.2 \pm 2.9	-103.2 \pm 1.2	8	0.932
C26	2016.00 \pm 0.10	293.1 \pm 40.5	14.7 \pm 2.0	-298.6 \pm 1.9	10	0.942
C27	2016.57 \pm 0.05	446.4 \pm 26.0	22.3 \pm 1.3	-295.6 \pm 9.9	15	0.980
C28	2016.69 \pm 0.07	306.1 \pm 23.4	15.3 \pm 1.2	-301.1 \pm 2.6	14	0.982
C29	2017.04 \pm 0.09	270.6 \pm 17.8	13.5 \pm 0.9	-311.0 \pm 1.9	16	0.972
C30	2017.51 \pm 0.22	272.2 \pm 98.0	13.6 \pm 4.9	-168.6 \pm 1.2	4	0.867
C31	2017.71 \pm 0.13	262.6 \pm 27.8	13.1 \pm 1.4	-343.7 \pm 1.9	13	0.961
C32	2018.05 \pm 0.24	241.1 \pm 131.9	12.1 \pm 6.6	-133.3 \pm 3.1	4	0.970
C33	2018.69 \pm 0.17	285.4 \pm 163.1	14.3 \pm 8.2	-293.5 \pm 14.4	4	0.734
C34	2019.41 \pm 0.13	135.1 \pm 7.3	6.8 \pm 0.4	-68.1 \pm 4.7	23	0.949
C35	2020.11 \pm 0.18	127.3 \pm 12.4	6.4 \pm 0.6	-38.1 \pm 2.8	19	0.970
C36	2020.47 \pm 0.69	66.0 \pm 21.8	3.3 \pm 1.1	-50.8 \pm 6.3	15	0.654

^a Number of epochs for which a given jet component was detected by our CE model fitting.

median reduced chi-squared value across all 203 epochs analysed in this work is approximately 1.2³, suggesting that our CE model-fitting in the image plane reasonably reproduces the complex visibility data of AO 0235+164.

3.1 Parsec-scale jet components in AO 0235+164

We have identified kinetically 36 non-static components in the parsec-scale jet of AO 0235+164, all of them moving with constant proper motions from the core⁴. Solid lines in the upper panel shown in Figure 2 represent linear regressions considering the equation

$$r(t) = \mu (t - t_0) , \quad (1)$$

where r is the core-component distance at the time t , while μ and t_0 are respectively the apparent proper motion and the ejection epoch of the jet components.

The kinematic parameters of these 36 jet components are listed in Table 1, together with the values of the Pearson correlation coefficient, r_{p} , for the linear regressions shown in Figure 2. The derived proper motions imply apparent speeds, β_{obs} , that range from $3.0c$ to $34.3c$ at the source's redshift, indicating substantial variations in their individual proper motions. Similar apparent velocities were found by Chu et al. (1996) through interferometric observations at 5 GHz from 1978.9 to 1983.5. Jorstad et al. (2017) estimated the apparent speeds for three jet components at 43 GHz, two of them compatible with our jet components C7 and C8. Using interferometric data at 43 GHz and based on the flare occurred between 2008 and 2010, Kutkin et al. (2018) identified a component with an apparent velocity equivalent to $\beta_{\text{app}} = (10.0 \pm 1.6)c$, which is compatible with the component C8 identified in this work.

³ Weaver et al. (2022) fitted the complex visibility data of AO 0235+164 between 2013 and 2018 using circular Gaussian components. Their model fittings resulted in a median reduced chi-square value of about 0.86, similar to the 0.96 found in our CE modellings in the uv -plane for the same interval.

⁴ We also fitted non-ballistic trajectories for those jet components with at least 9 epochs of detection, but no relevant differences between ballistic and non-ballistic fits were found considering the interval in which each of them is detected.

The instantaneous flux density of the jet components, F_ν , is shown in the bottom panel of Figure 2. This quantity is defined as

$$F_\nu = 8 \ln 2 \left[\frac{a^2 \sqrt{1 - \epsilon^2}}{(\Theta_{\text{beam}}^{\text{FWHM}})^2 \sqrt{1 - \epsilon_{\text{beam}}^2}} \right] I_0. \quad (2)$$

where $\Theta_{\text{beam}}^{\text{FWHM}}$ and ϵ_{beam} are respectively the FWHM major axis and eccentricity of the synthesised elliptical CLEAN beam of the observations.

The majority of the jet components exhibits either a systematic decrease of F_ν as time evolves (e.g., component C5), or an initial short phase where F_ν increases with time and a quasi-monotonic decrease of F_ν after reaching its maximum value (e.g., component C8). This behaviour is in agreement with predictions from the shock-in-jet models (e.g., Konigl 1981; Marscher & Gear 1985; Hughes et al. 1985; Valtaoja et al. 1992; Türler et al. 2000).

The mean position angle of each jet component in AO 0235+164, $\bar{\eta}$, also changes from component to component, reflecting on the spread over all quadrants on the plane of the sky shown in Figure 3. Notably, this unusual blazar jet behaviour had already been observed by Kutkin et al. (2018) in AO 0235+164 using a shorter monitoring dataset (2007–2016). Similar findings were reported by Weaver et al. (2022), who analysed radio maps from 2007 to 2017, and by Escudero Pedrosa et al. (2024) using data from 2008 to 2024.

3.2 Limits for the Lorentz factor and the jet viewing angle of AO 0235+164

The minimum relativistic jet Lorentz factor, γ_{\min} , can be calculated from the maximum apparent speed among the jet components identified kinematically, $\beta_{\text{app}}^{\text{max}}$, through

$$\gamma_{\min} = \sqrt{1 + (\beta_{\text{app}}^{\text{max}})^2}, \quad (3)$$

which implies $\gamma_{\min} = 34.3 \pm 6.6$ for the parsec-scale jet of AO 0235+164 after using the apparent speed of the jet component C22 as a proxy for $\beta_{\text{app}}^{\text{max}}$. This result is in good agreement with several previous estimates in the literature. Volvach et al. (2019a) derived a value of approximately 35 by analysing time delays between radio and gamma-ray flares, whilst Jorstad et al. (2017) found values of 28.6 ± 6.9 and 31.3 ± 4.9 for jet components B1 and B2, respectively. Similarly, Weaver et al. (2022) reported Lorentz factors of γ of 37.2 ± 5.8 , 39.4 ± 4.5 , and 31.6 ± 4.0 for components B1, B2, and B6. Earlier studies by O’Dell et al. (1988) and Qian et al. (2000) also proposed that $\gamma \gtrsim 25$.

Nevertheless, lower values for γ have also been suggested for AO 0235+164. Volvach et al. (2015a) reported a value of around 20, which is close to the $\gamma = 16.8^{+3.6}_{-3.1}$ found by Cheong et al. (2023). Furthermore, a value of $\gamma \approx 14$ was reported by both Kutkin et al. (2018) and Wang & Jiang (2020).

On the other hand, we can also derive a very conservative maximum value for the jet viewing angle, ϕ_{max} , from the lowest apparent speed, $\beta_{\text{app}}^{\text{min}}$, among detected jet components (e.g., Sumida et al. 2021)

$$\phi_{\text{max}} \approx \arccos \left[\frac{(\beta_{\text{app}}^{\text{min}})^2 - 1}{(\beta_{\text{app}}^{\text{min}})^2 + 1} \right], \quad (4)$$

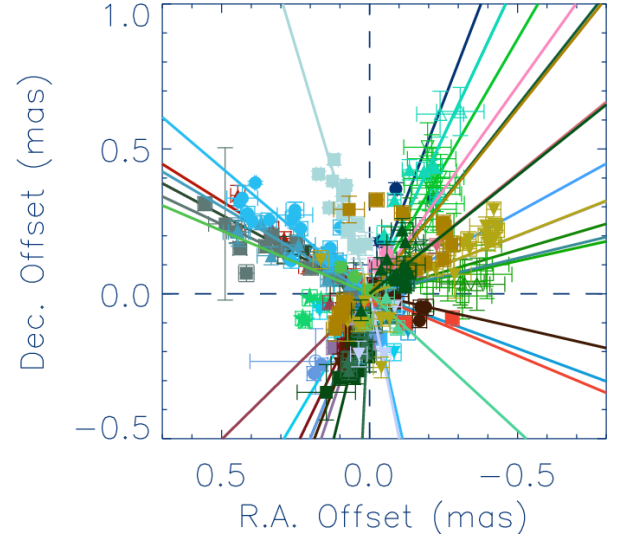


Figure 3. Right ascension and declination offsets of the 36 jet components identified in this work. Coloured straight lines represent their respective mean position angles, while dashed horizontal and vertical grey lines are used to mark the four quadrants of the sky. Same colour scheme of Figure 2 is adopted here.

leading to $\phi_{\text{max}} = 36.7 \pm 7.8$ (the apparent velocity of the jet component C3 was used in this calculation).

Estimates for the jet viewing angle of AO 0235+164 vary in the literature, though most analyses suggest a value of less than 4° . For instance, Volvach et al. (2015b) derived a value of between 2° and 3° , whilst a subsequent analysis by Volvach et al. (2019a) suggested a smaller angle of approximately 1.6° . Consistent with these findings, Agudo et al. (2011) established an upper limit of 2.4° .

Other analyses have indicated even smaller angles. Hovatta et al. (2009) found $\phi = 0.4^\circ$ (based on $\beta_{\text{app}} = 2c$ from Kutkin et al. 2018), and Kutkin et al. (2018) themselves reported a value of 1.7° . Cheong et al. (2023) reported a value of $1.42^{+1.07}_{-0.52}$. Furthermore, kinematic analysis of individual jet components has yielded a range of values from 0.2 ± 0.1 to 3.2 ± 0.7 (Jorstad et al. 2017; Weaver et al. 2022).

In contrast to these smaller angles, Wang & Jiang (2020) derived a much larger viewing angle of approximately 6° from their helical model for jet polarisation. However, the same study also derived $\phi = 1.7^\circ$ when assuming an apparent speed of $\beta_{\text{app}} = 10c$.

3.3 The brightness temperature of the core region

The brightness temperature of the core at the rest frame of the source, $T_{\text{B,rest}}$, can be calculated from

$$T_{\text{B,rest}} = (1 + z) \frac{2 \ln 2}{\pi k} \frac{c^2}{v^2} \frac{F_\nu}{a_{\text{FWHM}} b_{\text{FWHM}}}, \quad (5)$$

where k is the Boltzmann constant, and a_{FWHM} and b_{FWHM} are, respectively, the FWHM of the elliptical Gaussian components along the major and the minor axes. If the emitting region is unresolved angularly, the term $a_{\text{FWHM}} b_{\text{FWHM}}$ in Equation 5 must be replaced by d_{min}^2 , define as (Lobanov 2005):

$$d_{\text{min}} = \frac{2^{2-\sigma/2}}{\pi} \left[\pi \ln 2 \left(\Theta_{\text{beam}}^{\text{FWHM}} \right)^2 \sqrt{1 - \epsilon_{\text{beam}}^2} \ln \left(\frac{\text{SNR}}{\text{SNR} - 1} \right) \right]^{1/2},$$

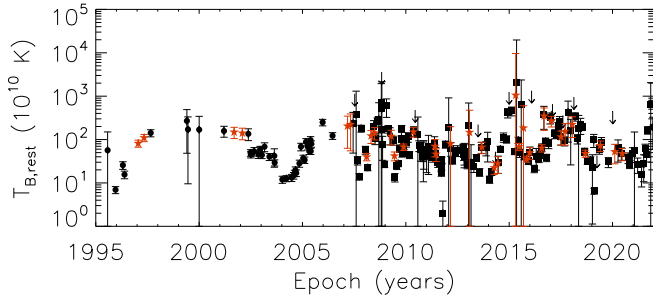


Figure 4. Brightness temperature of the core at the rest frame of AO 0235+164 as a function of time. Black circles and squares refer respectively to estimates at 15 and 43 GHz. Downward arrows correspond to upper limits (derived from Equation 6), while red stars represent the interpolated values of $T_{B,\text{rest}}$ at the ejection epochs of the jet components.

(6)

where SNR is the signal-to-noise ratio and ϖ is an index describing the weighting method used to generate the radio maps ($\varpi = 0$ for uniform weighting and $\varpi = 2$ for natural weighting; Lobanov 2005).

The time behaviour of the brightness temperature of the core region derived from Equation 5 is shown in Figure 4. We obtained for the core region at 15 GHz $0.07 \leq T_{B,\text{rest}} (10^{12} \text{ K}) \leq 2.85$, while for the data at 43 GHz, $0.07 \leq T_{B,\text{rest}} (10^{12} \text{ K}) \leq 21.88$. These values are compatible with those estimated in previous works (e.g., Lee et al. 2016; Homan et al. 2021), confirming the fact that AO 0235+164 can reach $T_{B,\text{rest}}$ as higher as 10^{13} K (Frey et al. 2000; Kutkin et al. 2018; Liodakis et al. 2018).

4 DISCUSSION

4.1 Changes in the apparent speed and brightness temperature

We presented in subsection 3.1 our results concerning the determination of the kinematic parameters of the parsec-scale jet components of AO 0235+164. As mentioned previously, their apparent speeds and position angles exhibit substantial changes during all the monitoring time analysed in this work. A pertinent question is which mechanism could be responsible for those changes? To answer it, it is necessary to recover the relationship between β_{obs} and the jet viewing angle, ϕ ,

$$\beta_{\text{obs}} = \frac{\beta \sin \phi}{(1 - \beta \cos \phi)}, \quad (7)$$

where $\beta = v/c$, v is the jet bulk speed. Introducing the relativistic Doppler boosting factor

$$\delta = \left[\gamma - (\gamma^2 - 1)^{1/2} \cos \phi \right]^{-1}, \quad (8)$$

where $\gamma = (1 - \beta^2)^{-1/2}$ is the jet Lorentz factor, we can rewrite Equation 7 as

$$\beta_{\text{obs}} = \delta \sqrt{\gamma^2 - 1} \sin \phi. \quad (9)$$

From Equation 9, it is clear that any change in β_{obs} implies a time-variable γ and/or ϕ .

In addition, the rest-frame brightness temperature of the core region also presents variability, as shown in Figure 4. The relationship between $T_{B,\text{rest}}$ and the intrinsic brightness temperature, $T_{B,\text{int}}$, is stated as (e.g., Readhead 1994; Kovalev et al. 2005; Homan et al. 2006):

$$T_{B,\text{rest}} = \delta T_{B,\text{int}}, \quad (10)$$

where $T_{B,\text{int}}$ is related to the equipartition temperature, $T_{B,\text{eq}} (\approx 5 \times 10^{10} \text{ K}; \text{Readhead 1994})$, through

$$T_{B,\text{int}} = \zeta^{2/17} T_{B,\text{eq}}, \quad (11)$$

where $\zeta = u_p/u_B$, the ratio between the energy density of the radiating particles, u_p , and the energy density of the magnetic field, u_B .

Substituting Equation 11 into Equation 10, we obtain

$$T_{B,\text{rest}} = \delta \zeta^{2/17} T_{B,\text{eq}}. \quad (12)$$

From Equation 12, we can realize that temporal changes in δ and/or ζ must drive variations in $T_{B,\text{rest}}$. In the former possibility, changes in γ and/or ϕ must occur, similar to what was inferred in the case of β_{obs} .

Isolating δ in Equation 12 and substituting it into Equation 9, we obtain

$$T_{B,\text{eq}} \frac{\beta_{\text{obs}}}{T_{B,\text{rest}}} = \frac{\sqrt{\gamma^2 - 1}}{\zeta^{2/17}} \sin \phi. \quad (13)$$

Note that the left-hand side of Equation 13 put together quantities that can be estimated (almost) directly from the interferometric data of AO 0235+164, while the right-hand side involves intrinsic quantities of the jet inlet region that are substantially harder to be inferred by the same data set. Note also that Equation 13 provides an additional probe for signatures of a possible parsec-scale jet precession in AO 0235+164, as we will discuss in the next section.

4.2 A precessing jet in AO 0235+164

Precession of the parsec-scale jet has already been invoked previously in the case of AO 0235+164, not only to explain quasi-periodic variability in its continuum (e.g., Kraus et al. 1999; Vol'vach et al. 2015a; Volvach et al. 2019b; Otero-Santos et al. 2023), but also to deal with changes in the jet position angle during decades of interferometric monitoring of this source at radio wavelengths (e.g., Zhang et al. 1997; Chen et al. 1999b; Escudero Pedrosa et al. 2024). Here, we revisited the scenario of the parsec-scale jet precession of AO 0235+164, using observational constraints from the longest interferometric monitoring of this source, as well as changes in its brightness temperature during this period.

The kinematic precession model adopted in this work was previously applied to other blazars (e.g. Abraham & Romero 1999; Abraham 2000; Caproni & Abraham 2004a,b; Caproni et al. 2013, 2017). It considers a relativistic jet with constant speed $v = \beta c$ ($0 \leq \beta < 1$), forming an angle ϕ in relation to the line of sight which is timely variable due to the precession motion of the jet. The jet precession occurs with a period $P_{\text{prec,obs}}$ inferred in the observer's reference frame, forming an apparent cone shape in which its axis forms an

angle ϕ_0 with respect to the line of sight. This apparent precession cone has a semi-opening angle φ_0 (an schematically view is shown in figure 1 in Caproni et al. 2009). Thus, precession induces periodic variations in ϕ that is quantified as (e.g., Caproni et al. 2017)

$$\cos \phi(\tau_s) = -e_{x,s}(\tau_s) \sin \phi_0 + \cos \varphi_0 \cos \phi_0, \quad (14)$$

where $\tau_s = t_s/P_{\text{prec},s}$, t_s is the inferred time at the source's reference frame, and $e_{x,s}(\tau_s)$ is given as

$$e_{x,s}(\tau_s) = \sin \varphi_0 \sin(\iota 2\pi \Delta \tau_s), \quad (15)$$

where ι is the precession direction ($\iota = 1$ for clockwise and $\iota = -1$ for counterclockwise sense), $\Delta \tau_s = \tau_s - \tau_{0,s}$, and $\tau_{0,s} = t_{0,s}/P_{\text{prec},s}$ is the precession phase (see Caproni et al. 2009 for more details).

A varying ϕ due to jet precession also introduces periodic modulations to the apparent velocities of the jet components (Equation 7), the relativistic Doppler boosting factor associated with the underlying jet (Equation 8) and the quantity $T_{B,\text{eq}} \frac{\beta_{\text{obs}}}{T_{B,\text{rest}}}$ (Equation 13), as well as to the jet's instantaneous position angle on the plane of the sky, η (e.g., Caproni et al. 2017):

$$\tan \eta(\tau_s) = \frac{A(\tau_s) \sin \eta_0 + e_{y,s}(\tau_s) \cos \eta_0}{A(\tau_s) \cos \eta_0 - e_{y,s}(\tau_s) \sin \eta_0}, \quad (16)$$

where $A(\tau_s)$ and $e_{y,s}(\tau_s)$ are defined respectively as

$$A(\tau_s) = e_{x,s}(\tau_s) \cos \phi_0 + \cos \varphi_0 \sin \phi_0, \quad (17)$$

and

$$e_{y,s}(\tau_s) = \sin \varphi_0 \cos(\iota 2\pi \Delta \tau_s). \quad (18)$$

The inferred time interval in the observer's reference frame, Δt_{obs} , is related to the elapsed time in the source's reference frame as

$$\frac{\Delta t_{\text{obs}}}{P_{\text{prec,obs}}} = \frac{\int_0^{\Delta \tau_s} \delta^{-1}(\tau) d\tau}{\int_0^1 \delta^{-1}(\tau) d\tau}. \quad (19)$$

In our purely kinematic precession model there are seven free parameters to be determined: ι , $P_{\text{prec,obs}}$, γ , η_0 , φ_0 , ϕ_0 and $\tau_{0,s}$. The last six free parameters were obtained via the CE method (Caproni et al. 2009, 2013) for both values of ι , and after fixing the range for the possible values that each of the free model parameters can assume. Regarding the jet bulk Lorentz factor, the CE optimization assumed values between 27.75 ($\beta = 0.999351$, corresponding to γ_{min} minus its one-sigma uncertainty) and 50.00 ($\beta = 0.9998$). For $P_{\text{prec,obs}}$, values ranged from 2.0 to 30 years, while the range between 0° to 40° 5 (ϕ_{max} plus its one-sigma uncertainty) was considered for ϕ_0 and φ_0 ⁵.

For the remaining free parameters, we assumed $-360^\circ < \eta_0 \leq 0^\circ$, since the jet components of AO 0235+164 spread across all sky quadrants and $0 \leq \tau_{0,s} < 1$.

⁵ During the whole CE optimization, if a given tentative solution has $\phi_0 + \varphi_0 > \phi_{\text{max}}$, both angles are automatically replaced to preserve the condition $\phi \leq \phi_{\text{max}}$ mentioned in subsection 3.2.

Having fixed the precession direction (ι), our CE method minimizes a merit function $S(k)$ at iteration k , which is defined as

$$S(k) = S_1(k) + S_2(k) + S_3(k), \quad (20)$$

where the individual terms $S_1(k)$, $S_2(k)$ and $S_3(k)$ are written as

$$S_1(k) = -\ln \left\{ \prod_{i=1}^{N_d} \frac{\exp \left[-\frac{1}{2} \left(S_{\alpha_i}^2(k) + S_{\delta_i}^2(k) + S_{r_i}^2(k) \right) \right]}{(2\pi)^{3/2} \sigma_{\Delta \alpha_i} \sigma_{\Delta \delta_i} \sigma_{\Delta r_i}} \right\}, \quad (21)$$

$$S_2(k) = -\ln \left\{ \prod_{i=1}^{N_{\text{kin}}} \frac{\exp \left[-\frac{1}{2} \left(S_{\beta_{\text{obs},i}}^2(k) + S_{\eta_i}^2(k) + S_{\beta'_{\text{obs},i}}^2(k) \right) \right]}{(2\pi)^{3/2} \sigma_{\beta_{\text{obs},i}} \sigma_{\eta_i} \sigma_{\beta'_{\text{obs},i}}} \right\}, \quad (22)$$

and

$$S_3(k) = -\ln \left\{ \prod_{i=1}^{N_{\text{TB}}} \frac{\exp \left[-\frac{1}{2} S_{\text{TB}_i}^2(k) \right]}{(2\pi)^{1/2} \sigma_{\text{TB}_i}} \right\}. \quad (23)$$

In the case of Equation 21, N_d is the total number of the Gaussian jet components found during the whole monitoring interval analysed in this work, and $\sigma_{\Delta \alpha_i}$, $\sigma_{\Delta \delta_i}$, and $\sigma_{\Delta r_i}$ correspond respectively the uncertainties in right ascension, declination, and core-component distance. Besides, $S_{\alpha_i}(k) = \sigma_{\Delta \alpha_i}^{-1} [\Delta \alpha_i - \Delta \alpha_{\text{mod}_i}(k)]$, $S_{\delta_i}(k) = \sigma_{\Delta \delta_i}^{-1} [\Delta \delta_i - \Delta \delta_{\text{mod}_i}(k)]$, $S_{r_i}(k) = \sigma_{\Delta r_i}^{-1} [\Delta r_i - \Delta r_{\text{mod}_i}(k)]$, $\Delta r_i^2 = \Delta \alpha_i^2 + \Delta \delta_i^2$, $\Delta r_{\text{mod}_i}^2 = \Delta \alpha_{\text{mod}_i}^2 + \Delta \delta_{\text{mod}_i}^2$, $\Delta \alpha_i$ and $\Delta \delta_i$ correspond to the displacements of the identified components of the jet i in relation to the core component, and $\Delta \alpha_{\text{mod}_i}$ and $\Delta \delta_{\text{mod}_i}$ correspond to the displacements of the identified jet components i predicted by the precession model (see equations 12 and 13 in Caproni et al. 2013 for the exact definitions of $\Delta \alpha_{\text{mod}_i}$ and $\Delta \delta_{\text{mod}_i}$).

In Equation 22, N_{kin} is the number of jet components kinetically identified in this work, $S_{\beta_{\text{obs},i}}(k) = \sigma_{\beta_{\text{obs},i}}^{-1} [\beta_{\text{obs},i} - \beta_{\text{obs},i}^{\text{mod}}(k)]$, $S_{\eta_i}(k) = \sigma_{\eta_i}^{-1} \tan [\eta_{\text{obs},i} - \eta_{\text{obs},i}^{\text{mod}}(k)]$, $S_{\beta'_{\text{obs},i}}(k) = \sigma_{\beta'_{\text{obs},i}}^{-1} [\beta'_{\text{obs},i} - \beta_{\text{obs},i}^{\text{mod}}(k)]$, $\beta_{\text{obs},i}$ and $\eta_{\text{obs},i}$ correspond respectively to the apparent velocity and position angle of the jet components on the plane of sky, to which $\sigma_{\beta_{\text{obs},i}}$ and σ_{η_i} correspond to their respective uncertainties. Primed and non-primed quantities in Equation 22 are given in terms of time (in the observer's reference frame) and position angle, respectively, with $\sigma_{\beta'_{\text{obs},i}} = \sqrt{\sigma_{\beta_{\text{obs},i}} \sigma_{\eta_i}}$.

Motivated by Sumida et al. (2021), who analysed the instantaneous behaviour of the core brightness temperature in other two blazars, we have included an additional observational constraint in relation to our previous works on jet precession. This third constraint is encoded in the term S_3 defined in Equation 23. The term S_3 involves T_{eq} , β_{obs} , and $T_{B,\text{rest}}$, estimated at the moments of jet component ejections (red points in Figure 4 calculated from spline interpolations). These three quantities are in the left side of Equation 13, remaining on its right side the parameters γ , ζ and ϕ . If these three last parameters do not change in time, $T_{B,\text{eq}} \beta_{\text{obs}} T_{B,\text{rest}}^{-1}$ is constant too, which is false in the case of AO 0235+164, as shown in Figure 5. Our kinematic jet precession model assumes a constant γ , such that changes in $T_{B,\text{eq}} \beta_{\text{obs}} T_{B,\text{rest}}^{-1}$ must be attributed to ζ and/or ϕ . We have assumed

Table 2. Precession model parameters optimized by our CE technique for clockwise and counter-clockwise senses of precession.

ι	$P_{\text{prec,obs}}$ (years)	γ	η_0 (deg)	ϕ_0 (deg)	φ_0 (deg)	$\tau_{0,s}$	ζ (10^5)	$S(k_{\text{max}})$ (10^4)
1	8.39 ± 0.24	29.2 ± 3.9	-26.7 ± 8.0	7.9 ± 2.6	9.3 ± 2.5	0.03 ± 0.51	1.0 ± 0.5	3.30
-1	6.00 ± 0.09	29.8 ± 4.0	-348.7 ± 12.9	6.2 ± 1.5	9.0 ± 0.8	0.79 ± 0.29	1.0 ± 0.3	6.42

Notes: The uncertainties in each parameter are at 1σ -level; Merit function in the final iteration ($k_{\text{max}} = 65$) is shown in the ninth column of this table.

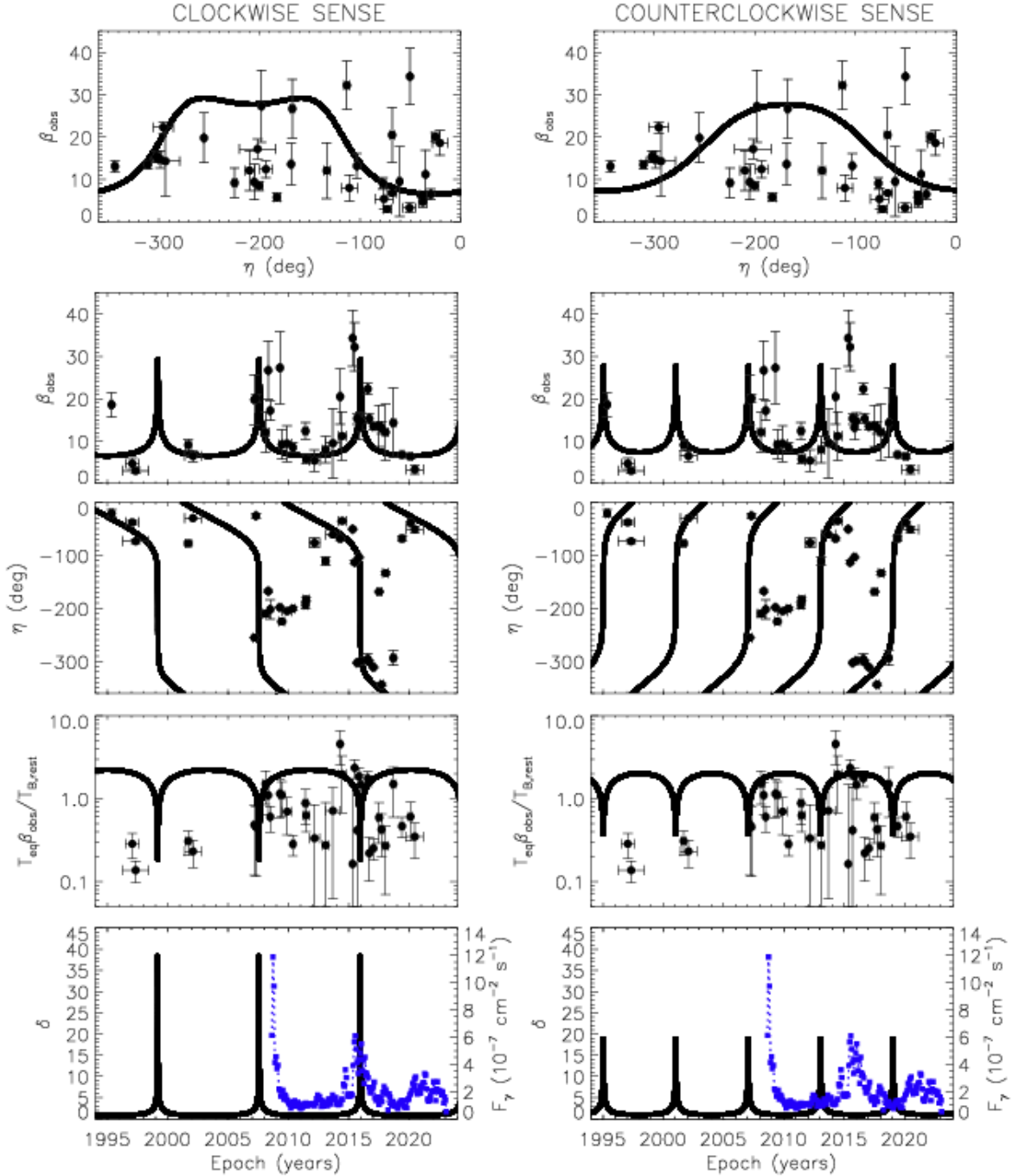


Figure 5. Jet precession models for AO 0235+164 obtained via the CE method considering clockwise and counter-clockwise senses of precession (left and right panels, respectively). Solid lines represent the predictions of the precession models given in Table 7 in the time-independent $\beta_{\text{obs}} - \eta$ plane (top panels), while time behaviour of these two quantities are shown in the middle panels. Black circles refer to the kinematic parameters of the jet components listed in Table 1. Bottom panels show the temporal behaviour of the dimensionless quantity $T_{\text{B,eq}}\beta_{\text{obs}}T_{\text{B,rest}}^{-1}$, and the Doppler factor (black line) superimposed on the public *Fermi* γ -ray light curve (blue squares).

that ζ remains constant throughout the period considered in this work to simplify our precession modellings. This assumption made us consider ζ as the eighth free parameter in our precession model, to be optimised by the CE technique. During CE optimisations, ζ was allowed to vary from 10^{-10} ($u_p \ll u_B$) to 10^5 ($u_p \gg u_B$).

The results from the CE optimisation for both clockwise and counter-clockwise senses of jet precession are shown in Figure 5, while the respective optimized precession parameters are given in Table 2. The parameters γ , ϕ_0 and φ_0 obtained at clockwise and counter-clockwise senses agree each other considering their respective uncertainties. The precession period at the observer's reference frame for the clockwise sense corresponds to 8.39 years, a slightly longer than 6.00 years found in the case of counter-clockwise precession. The precession period of 8.4 years is compatible with the periodicity of about 8 years detected in the optical light curve of AO 0235+164 (Raiteri et al. 2006; Fan et al. 2016b, 2017; Roy et al. 2022). On the other hand, the counter-clockwise precession period of 6.0 years is compatible with a periodicity of 5-6 years identified at radio frequencies (Roy et al. 2000; Liu et al. 2006; Fan et al. 2007a; Tripathi et al. 2021) and optical bands (Raiteri et al. 2001; Fan et al. 2002).

Both jet precession models reasonably fit the observational data set, with the clockwise precession being slightly favoured when considering the final value of the merit function, $S(k_{\max})$, as shown in Table 2. Coincidence between the two main gamma-ray flares seen in the public *Fermi* light curve of AO 0235+164 and the peaks of the Doppler factor predicted by the clockwise jet precession represents an additional advantage over the counter-clockwise precession (see the bottom panels in Figure 5). However, the values of $S(k_{\max})$ differ by less than a factor of two, which implies the counter-clockwise sense of precession for AO 0235+164 cannot be ruled out at all.

Although jet precession can roughly provide the correct amplitude variation of $T_{B,\text{eq}}\beta_{\text{obs}}T_{B,\text{rest}}^{-1}$, additional fluctuations are seen in Figure 5, suggesting that ζ might have also varied during this interval. Indeed, it is perfectly acceptable since a switch between low and high brightness temperature states must be related to changes in the energy densities of the particles and/or the magnetic field (e.g., Homan et al. 2006).

Some jet components with apparent velocities of about $10c$ and position angles around -200° are systematically below the curves representing our precession models in the $\beta_{\text{obs}} - \eta$ plots shown in Figure 5. Additional oscillations superimposed on the jet precession might explain this discrepancy (see subsection 5.2).

5 A SUPERMASSIVE BINARY BLACK HOLE SYSTEM IN AO 0235+164

The existence of a SMBHB in the nucleus of AO 0235+164 has been proposed in the literature, based mainly on the quasi periodic variability detected in its radio and optical continuum light curves (e.g., Chen et al. 1999b; Liu et al. 2006; Vol'vach et al. 2015a; Bychkova et al. 2015; Wang et al. 2017; Volvach et al. 2019b; Roy et al. 2022; Otero-Santos et al. 2023).

Chen et al. (1999b) estimated a lower limit of $1.46 \times 10^8 M_\odot$ for the total mass of the SMBHB in AO 0235+164 after interpreting the periodicities of 1.81 and 3.63 years found in its single-dish flux density at 5 GHz. Liu et al. (2006) found six quasi-periodic oscillations in the radio light curves of AO 0235+164, attributing them to oscillatory accretion rates due to acoustic p -mode oscillations (e.g., Rezzolla et al. 2003; Rubio-Herrera & Lee 2005) in a geometrically thick disc probably induced by a SMBHB with a total mass of $4.7 \times 10^8 M_\odot$.

Vol'vach et al. (2015a) and Volvach et al. (2019b) found periodicities of about two and eight years in a multi-wavelength analysis of AO 0235+164, which were interpreted respectively as the orbital and jet precession periods in a SMBHB of $\sim 10^{10} M_\odot$. Roy et al. 2022 suggested a binary system of supermassive black holes as an explanation for the major flares in the R -band light curve of AO 0235+164 are double-peaked, with the secondary peak following the primary by about 2 years, a similar behaviour observed in the case of the blazar OJ 287 (e.g., Lehto & Valtonen 1996).

In this section, we analyse the possibility of the parsec-scale jet precession in AO 0235+164 is driven by a secondary supermassive black hole (SMBH) with mass M_s in a non-coplanar circular orbit of radius d_{BH} around a primary SMBH with mass M_p (e.g. Sillanpaa et al. 1988; Katz 1997; Abraham 2000; Romero et al. 2000; Caproni & Abraham 2004b,a; Caproni et al. 2006, 2013; Roland et al. 2013; Caproni et al. 2017; Nandi et al. 2021; Sebastian et al. 2024), assuming that its jet comes from the primary accretion disc torqued by the secondary SMBH. Some consequences of this scenario on the periodic variabilities found in the continuum emission of this source is also explored in this particular section. Note also that all the results presented hereafter are based only on the clockwise jet precession model discussed in subsection 4.2 without loss of generality, since the choice of the counter-clockwise jet precession parameters does not alter substantially the physical characteristics of the putative SMBHB in AO 0235+164.

5.1 Physical parameters of the SMBHB

Considering the formalism provided in Bate et al. (2000), as well as assuming an accretion disc with a power-law surface density distribution, we can write a relationship between the precession period of the accretion disc/jet, $P_{\text{prec},s}$, and the orbital period of the secondary BH, $P_{\text{orb},s}$, both given at the source's reference frame, as follows (e.g., Sebastian et al. 2024)

$$[K(s) \cos \varphi_0] \left(\frac{P_{\text{prec},s}}{P_{\text{orb},s}} \right) = \left[\frac{(1 + q_{\text{BH}})^{1/2}}{q_{\text{BH}}} \right] \left(\frac{R_{\text{out},p}}{d_{\text{BH}}} \right)^{-3/2}, \quad (24)$$

where $q_{\text{BH}} = M_s/M_p$, $R_{\text{out},p}$ is the outer radius of the primary disc, and $K(s) \approx 0.19 - 0.47$ for a power-law surface density accretion disc with an index s between 0 and -2 (Larwood et al. 1996; Bate et al. 2000).

Using the third Kepler's law, Equation 24 can be rearranged to obtain $P_{\text{orb},s}$ in terms of q_{BH} after fixing the values of s , φ_0 , $P_{\text{prec},s}$ and $R_{\text{out},p}$:

$$P_{\text{orb},s} = \sqrt{2\pi K(s) \cos \varphi_0 P_{\text{prec},s} \sqrt{\frac{R_{\text{out},p}^3}{G M_{\text{BH}}}} \frac{q_{\text{BH}}}{\sqrt{1 + q_{\text{BH}}}}}, \quad (25)$$

where G is the gravitational constant, $M_{\text{BH}} (= M_s + M_p)$ is the total mass of the SMBHB.

We show in Figure 6 the behaviour of $P_{\text{orb},s}$ as a function of q_{BH} for three generic values of $R_{\text{out},p}$: 0.1, 0.01 and 0.001 pc. In those calculations, it was assumed $M_{\text{BH}} = 10^{8.54 \pm 0.12} M_\odot$, the mean value considering the estimates found in the literature (Fan et al. 2000; Liu et al. 2006; Paliya et al. 2021; Roy et al. 2023), and $P_{\text{prec},s} = 4.32 \pm 0.12$ yr, suitable for a ballistic jet precession scenario (e.g., Rieger 2004; Abraham & Romero 1999; Abraham 2000; Caproni & Abraham 2004a,b).

The precession period of the primary disc and its relationship

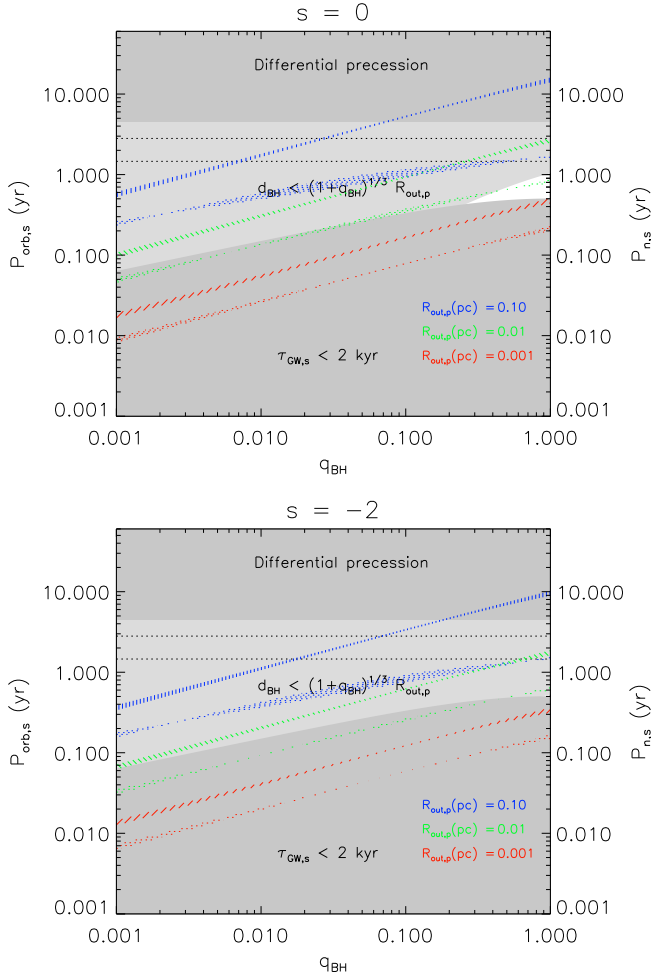


Figure 6. Orbital period of the secondary BH and nodding period as a function of q_{BH} for a primary accretion disc with a constant surface density ($s = 0$, top panel) and a decreasing surface density ($s = -2$, bottom panel) in the ballistic jet precession scenario ($P_{\text{prec},s} = 4.32$ yr). Slanted hatched stripes refer to the orbital period of the secondary BH considering outer radii for the primary disc of 0.1 pc (blue colour), 0.01 pc (green colour) and 0.001 pc (red colour) at 1σ -level calculated from Equation 25. Dotted stripes show the behaviour of the nodding period for the same three values of the outer radii. The dotted horizontal lines correspond to the periodicities of 2.8 and 5.4 years detected in the radio and optical light curves of AO 0235+164 converted to the source's reference frame. Dark gray regions delimitate the non-solid body precession regime and BH separations that lead to gravitational-wave time-scales in the source's reference frame shorter than 2000 years. The light gray region implies a BH separation that is smaller than about the outer radius of the primary disc. Viable solutions are found in the white region of the plots.

with the orbital period of the misaligned secondary BH, as given in Equation 25, assumes that the disc precesses rigidly, implying that the orbital period of the secondary BH must be shorter than the precession period, as well as the former quantity must be longer than the orbital period at the outer radius of the primary disc, $P_{\text{out},p}$ (Bate et al. 2000). The first requirement ($P_{\text{prec},s} \gg P_{\text{orb},s}$) requires that acceptable orbital periods must be below of the upper rectangular dark grey region labelled as ‘Differential precession’ in the two panels of the Figure 6. The second requirement ($P_{\text{orb},s} \gg P_{\text{out},p}$) produces an exclusion region shown in the same panels as a light grey region labelled as ‘ $d_{\text{BH}} < (1 + q_{\text{BH}})^{1/3} R_{\text{out},p}$ ’.

A third requirement that must be fulfilled is the stability of the

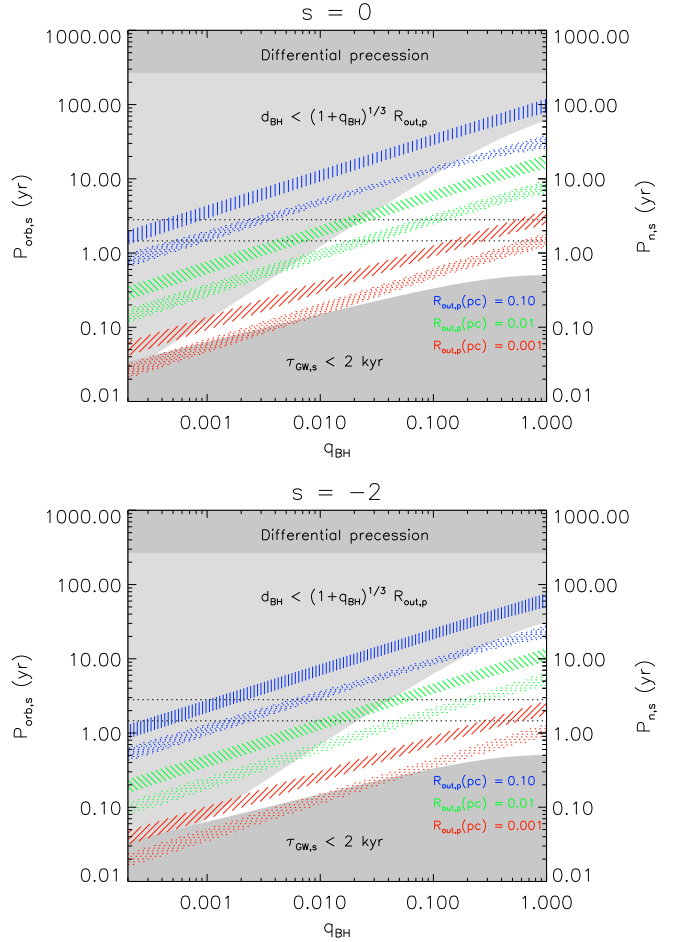


Figure 7. The same plots shown in Figure 6 but considering a non-ballistic jet precession scenario ($P_{\text{prec},s} = 188$ yr).

binary system against gravitational wave losses. From the time-scale of the gravitational waves in the source's reference frame, $\tau_{\text{GW},s}$ (e.g., Shapiro & Teukolsky 1983), the shortest orbital period of the secondary SMBH, $P_{\text{orb},s}^{\text{min}}$, to avoid the coalescence of the SMBHB within an interval of $\tau_{\text{GW},s}$ can be determined from

$$P_{\text{orb},s}^{\text{min}} \geq 2\pi \left[\frac{256}{5c^5} (GM_{\text{BH}})^{5/3} \frac{q_{\text{BH}}}{(1 + q_{\text{BH}})^2} \tau_{\text{GW},s} \right]^{3/8}. \quad (26)$$

In Figure 6, the region where $\tau_{\text{GW},s} \leq 2000$ yr is represented by the bottom dark grey zone labelled as ‘ $\tau_{\text{GW},s} < 2$ kyr’. This particular choice for $\tau_{\text{GW},s}$ implies in a relative change of $P_{\text{orb},s}$ of smaller than **2 percent** during the last 100 years, smaller than the estimated uncertainty for $P_{\text{prec},s}$. It assures a time-steady accretion disc/jet precession in AO 0235+164 independent of the chosen values of s and q_{BH} during almost thirty years of interferometric monitoring of this source considered in this work.

The allowed combinations among $R_{\text{out},p}$, s and q_{BH} that lead to $P_{\text{orb},s}$ compatible with the inferred jet precession period in AO 0235+164 are found in the white region in Figure 6. We can realize that no reasonable solution has been found for $s = -2$ ⁶. For

⁶ Either $s \gtrsim -1.8$ or $\tau_{\text{GW},s} \lesssim 1.7$ kyr are necessary conditions to provide acceptable solutions considering the ballistic jet precession scenario.

$s = 0$, orbital periods roughly between 0.5 and 1 yr are allowed in this source, implying in a separation between the primary and secondary black holes ranging from about 2 to 4 mpc (0.25–0.51 μ as). Moreover, $R_{\text{out,p}}$ must be ranged between 1 and 3 mpc, as well as $q_{\text{BH}} \gtrsim 0.3$.

The inferred range for the separation between the primary and secondary black holes in AO 0235+164 are not angularly resolved by VLBI experiments currently available. However, a SMBHB is expected to emit gravitational waves at a frequency corresponding to twice the orbital frequency in a circular orbit (e.g., Peters & Mathews 1963; Press & Thorne 1972). For $P_{\text{orb,s}}$ between 0.5 and 1 yr estimated, gravitational waves are respectively generated between 31.7 and 15.8 nHz. Such frequencies are outside of the range planned to be covered by the Laser Interferometer Space Antenna (LISA; Amaro-Seoane et al. 2017), but accessible for experiments like the Pulsar Timing Arrays (PTAs; e.g., EPTA Collaboration et al. 2023 and references therein) in full operation. The detection of gravitational radiation in such frequency range could confirm the presence of a SMBHB in the core of AO 0235+164.

The 36 jet components identified kinematically in this work exhibit proper motions that are consistent with ballistic displacements. However, several of these components (namely C5, C14, C16, C18, C27, C29, C34, C35 and C36) display a relatively high scatter around the receding motions predicted by the ballistic scenario. Although fitting non-ballistic trajectories to these components did not yield significant differences compared with the ballistic model over the interval during which they were observed by the VLBI experiments, their backward or forward extrapolations could result in measurable discrepancies between these two scenarios. It should be noted that accelerated motions may arise either from intrinsic variations in the jet Lorentz factor or from changes in the three-dimensional orientation of the jet as it propagates (e.g. Homan et al. 2009).

In the case of jet precession involving non-ballistic motions, light-travel time effects shorten the precession period measured in the observer's reference frame (e.g., Rieger 2004). Assuming that the inferred jet precession parameters in this work still hold, light-travel time effects implies $P_{\text{prec,s}} = 188 \pm 77$ yr, which was derived from (e.g., Romero et al. 2003; Caproni et al. 2013, 2017)

$$P_{\text{prec,s}} = \frac{P_{\text{prec,obs}}}{(1+z)(1-\beta \cos \varphi_0 \cos \phi_0)}, \quad (27)$$

also considering the values of $P_{\text{prec,obs}}$, φ_0 and ϕ_0 listed in Table 2 for the clockwise sense of precession.

Following the same approach described below, we present in Figure 7 the results considering the non-ballistic jet precession scenario for AO 0235+164. As expected, the ranges for viable values of $P_{\text{orb,s}}$ and q_{BH} clearly widen in comparison with those found assuming ballistic precession as shown in Figure 6, implying $0.05 \text{ yr} \lesssim P_{\text{orb,s}} \lesssim 60 \text{ yr}$ and $q_{\text{BH}} \gtrsim 0.0004$. Besides, d_{BH} must be between 0.0004 and 0.05 pc (0.05–6.32 μ as), $R_{\text{out,p}}$ between 0.0004 and 0.06 pc, and gravitational-wave frequencies between about 0.3 and 317 nHz.

5.2 Nodding motions

Besides the precession of the primary accretion disc in a SMBHB with the secondary BH revolving in a misaligned orbit, Katz et al. (1982) showed that short-term oscillations (nodding motions) about the mean precession motion can occur, with an period $P_{\text{n,s}}$ defined as

$$P_{\text{n,s}} = \frac{1}{2} \left(P_{\text{orb,s}}^{-1} + P_{\text{prec,s}}^{-1} \right)^{-1}, \quad (28)$$

where the retrograded nature of the disc precession was already considered in Equation 28 (e.g., Katz 1997 for further details).

The predicted values for $P_{\text{n,s}}$ from Equation 28 are also plotted in Figure 6 and Figure 7. Considering the allowed values for the orbital period of the secondary BH, only non-ballistic precession scenario admits nodding motion of the jet, with $P_{\text{n,s}}$ ranging roughly from 0.07 yr to 20 yr. Such periodic modulations introduce an additional oscillation about the precession motion of the disc/jet with an intrinsic amplitude, φ_{n} , given as (e.g., Katz 1997)

$$\varphi_{\text{n}} = \frac{P_{\text{n,s}}}{P_{\text{prec,s}}} \tan \varphi_0, \quad (29)$$

resulting in φ_{n} roughly between $0^\circ.003$ to $1^\circ.0$ for AO 0235+164.

The impact of nodding oscillations on β_{obs} and η can be quantified substituting φ_0 by $\varphi_0 \pm \varphi_{\text{n}}$ in Equation 15 and Equation 18. Negligible effects on β_{obs} and η are obtained considering $\varphi_{\text{n}} \sim 0^\circ.003$. However, the upper limit of about $1^\circ.0$ for φ_{n} introduces changes in β_{obs} ranging approximately from $-16.0c$ to $1.6c$. These extreme values occurs when the jet is closer to the line of sight ($\phi \lesssim 4^\circ$), while amplitude changes lower than $0.4c$ are expected for $\phi \gtrsim 15^\circ$ considering our best precession model ($P_{\text{prec,obs}} = 8.39$ years). In the case of η , oscillations between -31° and 31° around the jet position angle due to precession are expected when the jet is closer to the line of sight, reducing to less than 2° for $\phi \gtrsim 15^\circ$. Interestingly, there are a bunch of jet components with $\eta \sim 200^\circ$ and $\beta_{\text{obs}} \sim 10c$ that are systematically below of the predictions from our jet precession models in the $\beta_{\text{obs}} - \eta$ plots shown in Figure 5. This particular value of position angle occurs when the jet is closer to the line of sight ($\phi \sim 1^\circ.4$), exactly when the nodding oscillations can reach their largest amplitudes. Indeed, a decrease of $16c$ in β_{obs} would be enough to reconcile our jet precession models with the apparent speeds of those components, even though a variation of 31° in η is not capable of reconciling model and the mean position angles of the jet components by itself. Therefore, the imprints of the nodding motions might be present in the kinematic of the parsec-scale jet components of AO 0235+164. Further analyses including nodding oscillations in the framework of jet precession are necessary to confirm it, as well as the high-cadence interferometric monitoring of the jet activity in this source.

5.3 Short-term periodicities and the SMBHB in AO 0235+164

As mentioned anteriorly, several periodicities in the continuum light curves of AO 0235+164 have been reported in the literature. The 8-yr periodicity at optical wavelengths may be attributed to the periodic Doppler factor changes driven by the parsec-scale jet precession happening in a clockwise sense. Moreover, the most powerful flares seen at γ -rays coincides in time with the highest values of the Doppler boosting factor in our best precession model (bottom-left panel in Figure 5), reinforcing such geometrical interpretation for the 8-yr periodicity.

At radio frequencies, periodicities between 2 and 3 years are often, with an optical counterpart of 2.95 years also reported in Fan et al. (2002). Similar behaviour is found for periodic variabilities occurring at a time-scale of 5–6 years. It is worth to verify whether both periodicities could be accommodated simultaneously in the SMBHB scenario responsible for the jet precession in AO 0235+164. The main

idea is to link those common short-term periodicities to the secondary black hole's orbital period and the jet's nodding motion. To better quantify it, we chose the periods 5.4 and 2.8 determined by [Liu et al. \(2006\)](#)⁷ as representative of such periodicities in the light curve of this source. We converted these periods to their values at the source's reference frame, indicating them by the dotted horizontal lines in the two panels of [Figure 7](#). Comparing them with the predicted orbital and nodding periods, tighter ranges for q_{BH} and $R_{\text{out,p}}$ are obtained: $0.04 \lesssim q_{\text{BH}} \lesssim 1$ and $0.001 \lesssim R_{\text{out,p}}(\text{pc}) \lesssim 0.007$ for $s = 0$, and $0.1 \lesssim q_{\text{BH}} \lesssim 1$ and $0.002 \lesssim R_{\text{out,p}}(\text{pc}) \lesssim 0.007$ for $s = -2$. Therefore, the SMBHB scenario explored in this work, together with a **non-ballistic** jet precession are able to provide a physical interpretation for three periodicities in the light curves of AO 0235+164.

6 ALTERNATIVE SCENARIOS

In the preceding section, we examined the feasibility of a SMBHB, wherein the secondary SMBH orbits the primary in a non-coplanar plane relative to the primary accretion disc, as a potential explanation for the precession of the parsec-scale jet in AO 0235+164. However, it is not the only mechanism capable of driving jet precession in astrophysical objects. In addition, the data scattering around the predictions from the CE-optimized jet precession models in [Figure 5](#) (particularly in the β_{obs} versus η plots) suggests possible additional or alternative scenarios not considered previously in this work, such as intrinsic curved jet trajectories, warped accretion disc instabilities, and Lense-Thirring precession. Here, we explore such possibilities in the context of AO 0235+164.

6.1 Geodetic precession

This mechanism also involves the presence of a SMBHB in the core of AGNs. Originally proposed for binary pulsars in our Galaxy (e.g., [Barker & O'Connell 1975](#)), the geodetic precession must occur when there is a misalignment between the spin axis of the primary and/or secondary SMBH and the direction of orbital angular momentum of the binary system. If the jet is aligned with the spin axis of one of the SMBHs, it will also precesses at a period $P_{\text{prec}}^{\text{geo}}$ (e.g. [Krause et al. 2019](#)):

$$\left(\frac{P_{\text{prec}}^{\text{geo}}}{\text{Myr}} \right) \cong 124 \frac{(1 + q_{\text{BH}})^2}{q_{\text{BH}}(3q_{\text{BH}} + 4)} \left(\frac{d_{\text{BH}}}{1\text{pc}} \right)^{5/2} \left(\frac{M_{\text{BH}}}{10^9 M_{\odot}} \right)^{-3/2}, \quad (30)$$

considering a circular orbit.

In the case of AO 0235+164, an upper limit for d_{BH} can be derived from [Equation 30](#) by setting $q_{\text{BH}} = 1$ and adopting $M_{\text{BH}} = 10^{8.54 \pm 0.12} M_{\odot}$. Assuming a geodetic (non-ballistic) precession period of $P_{\text{prec}}^{\text{geo}} \sim 188$ years, we obtain $d_{\text{BH}} \lesssim 3.1$ mpc, which yields $\tau_{\text{GW},s} \sim 5251$ yr. This suggests that the SMBHB would remain stable against gravitational-wave losses if geodetic precession is indeed responsible for the jet precession in AO 0235+164. By contrast, for ballistic precession with $P_{\text{prec}}^{\text{geo}} \sim 4.32$ yr, we find $d_{\text{BH}} \lesssim 0.7$ mpc and $\tau_{\text{GW},s} \sim 13$ yr, indicating that the SMBHB would be unstable to gravitational-wave losses in this scenario.

⁷ [Liu et al. \(2006\)](#) also considered a SMBHB as a natural candidate for explaining the six quasi-periodic oscillations that they detected at radio light curves of AO 0235+164.

6.2 Warped accretion disc by the Lense-Thirring effect

Frame dragging produced by a Kerr black hole causes precession of a particle if its orbital plane is inclined in relation to the equatorial plane of the black hole. The precession angular velocity Ω_{LT} due to the Lense-Thirring effect (LT) is defined as ([Lense & Thirring 1918](#)):

$$\Omega_{\text{LT}}(r) = \frac{2G}{c^2} \frac{J_{\text{BH}}}{r^3}, \quad (31)$$

where r is the radial distance from the spinning SMBH with an angular momentum, J_{BH} ,

$$J_{\text{BH}} = a_* \frac{GM_{\text{BH}}^2}{c}, \quad (32)$$

where a_* is a dimensionless parameter ranging from -1 to 1, defined as the ratio of the angular momentum of the compact object and that of a Kerr black hole rotating at its maximal velocity.

Besides precession of the angular momenta of the spinning SMBH and the disc around the total angular momentum of the system, the combined influence of the LT effect and the internal viscosity of the accretion disc also induces an alignment (or counteralignment in some cases; e.g. [King et al. 2005](#); [Lodato & Pringle 2006](#)) between the angular momenta of a Kerr SMBH and its accretion disc. This phenomenon, referred to as the Bardeen-Petterson effect (BP) ([Bardeen & Petterson 1975](#)), predominantly affects the innermost regions of the disc, as the LT effect operates over a limited range due to its dependence on r^{-3} . In contrast, the outer regions of the accretion disc generally retain their original orientation. The boundary between these two regions, known as the Bardeen-Petterson radius, R_{BP} , is primarily determined by the physical characteristics of the accretion disc (e.g. [Kumar & Pringle 1985](#); [Ivanov & Illarionov 1997](#); [Nelson & Papaloizou 2000](#)), with this transition occurring smoothly.

The shape of a steady-state accretion disc under BP torques was derived analytically by [Scheuer & Feiler \(1996\)](#) under the assumption of a disc with constant surface density and constant viscosities acting azimuthally and vertically along it. [Martin et al. \(2009\)](#) extended the Scheuer & Feiler's results to the case where viscosities and surface densities are power laws in the distance from the SMBH, while [Chen et al. \(2009\)](#) also considered power-law viscosities with indices not necessarily equal. The alignment and precession time-scales were also calculated by [Scheuer & Feiler \(1996\)](#) and [Martin et al. \(2009\)](#) assuming an infinite outer disc radius (or an outer radius much larger than the BP (warping) radius; see Section 5 in [Martin et al. 2009](#) for further information). [Nandi et al. \(2021\)](#) and [Sebastian et al. \(2024\)](#) showed that the precession periods of their sample of radio galaxies are fully compatible with those expected from a steady-state BP accretion disc as described by [Martin et al. 2009](#). However, this formalism predicts much longer precession time-scales ($\gtrsim 10^6$ years) than the jet precession period of 4.32 years (or ~ 188 years for the non-ballistic precession) estimated for AO 0235+164 in this work. In these calculations, we employed equations (54) and (57) from [Martin et al. \(2009\)](#), along with estimates for the surface density of a power-law accretion disc, following the approach of [Caproni et al. \(2006\)](#). We have also assumed a dimensionless viscosity parameter, α ([Shakura & Sunyaev 1973](#)), equal to 0.1, and a bolometric luminosity of $7 \times 10^{-3} L_{\text{Edd}}$ ([Liu et al. 2006](#)), where L_{Edd} denotes the Eddington luminosity in those calculations.

Although numerical simulations have confirmed the classical configuration of a BP accretion disc (e.g. [Nelson & Papaloizou 2000](#); [Lodato & Pringle 2007](#); [Lodato & Price 2010](#); [Nixon & King 2012](#);

Liska et al. 2018), this picture can be fundamentally altered by strong magnetic fields, non-linear effects arising from high inclination angles between the angular momenta of the SMBH and the disc, or for a disc in a low-viscosity regime. Considering non-linear fluid dynamics of an warped accretion disc (e.g. Ogilvie 1999, 2000), Nixon & King (2012) found that when $\alpha \lesssim 0.3$ and the initial angle of misalignment between the disc and hole is $\gtrsim 45^\circ$, frame dragging by the Kerr BH tears the disc apart into differentially precessing smaller discs. For a smaller tilted angle of about 30° , the disc breaking could happen for a low-viscosity regime ($\alpha \ll 0.2$). Numerical simulations corroborate the possibility of a disc be broken in individual small independent (precessing) discs by the Lense-Thirring effect induced by a single black hole (e.g., Lodato & Pringle 2006; Nixon et al. 2012; Nealon et al. 2015; Liska et al. 2021; Raj et al. 2021; Drewes & Nixon 2021; Musoke et al. 2023; Kaaz et al. 2023).

Analytical estimates for the upper limit of the radius where the accretion disc can break, R_{break} , were firstly derived in a diffusive and wave regimes by Nixon et al. (2012) and Nealon et al. (2015), respectively. In practice, this upper limit depends on several parameters (e.g., α , disc's aspect ratio, black hole spin, etc.), but for reasonable values a minimum initial tilt angle of the order of one degree can be obtained (Nixon et al. 2012; Nealon et al. 2015). The precession angle of about 9° found in this work (Table 2) is barely above this theoretical lower limit, which means the tearing of the accretion disc might occur in AO 0235+164.

For a disc tilted by $\sim 9^\circ$, the (theoretical) breaking radius must occur at a distance smaller than about one thousand gravitational radius for $\alpha \sim 0.01 - 0.3$ and disc's aspect ratio between 0.001 and 0.1, depending on the SMBH spin. Assuming that the inner disc formed by the tearing process is precessing rigidly due to the LT effect, we can use the formalism introduced by Liu & Melia (2002) to check whether the jet precession period inferred in this work is compatible with this scenario. Caproni et al. (2004) analysed the possibility of the spin-induced precession in a small sample of AGNs and in Sgr A*, calculating the ratio $P_{\text{prec},s}/M_{\text{BH}}$ as a function of a_* . In the case of AO 0235+164, $P_{\text{prec},s}/M_{\text{BH}} \sim 5.4 \times 10^{-7} \text{ yr } M_\odot^{-1}$ for the non-ballistic jet precession scenario or $P_{\text{prec},s}/M_{\text{BH}} \sim 1.2 \times 10^{-8} \text{ yr } M_\odot^{-1}$ for the ballistic one, implying in a conservative value for the outer radius of the inner disc smaller than about some thousands of gravitational radius, $R_g (= GM_{\text{BH}}/c^2)$ (see figure 1 in Caproni et al. 2004). It is in fair agreement with the predicted upper limit for the breaking radius in AO 0235+164 ($\lesssim 1000 R_g$), suggesting the feasibility of the spin-induced precession acting upon a broken accretion disc in this blazar.

Note that the LT effect and torques generated in a SMBHB may co-exist (including in AO 0235+164), bringing much more complexity to the evolution of accretion discs in such systems. Nixon et al. (2013) analysed the case of a circumbinary accretion disc that is misaligned to the orbital plane of a SMBHB and found that discs are susceptible to tearing for almost all tilt angles. Hayasaki et al. (2015) extended such analyses to the case of a SMBHB in a eccentric orbit. Tremaine & Davis (2014) explored the dynamics of warped accretion discs around BHs, focusing on the interplay of various torques, including LT, viscous torques, companion, and self-gravitational torques. Doğan et al. (2015) showed that tilted discs inside a binary system are susceptible to tearing from the outside in, because of the gravitational torque from the secondary (no LT torques are included in the calculations). From 1D numerical calculations, Gerosa et al. (2020) studied the non-linear dynamics of warped accretion discs under the influence of both relativistic frame dragging and binary companion. One of the results they found was the angular momentum of each BH

either achieve complete alignment with the angular momentum of the disc or reach a critical obliquity, beyond which stationary solutions cease to exist, leading to a broken disc. Hydrodynamical simulations by Nealon et al. (2022) corroborate those findings, also showing that when disc breaks, the ability of BHs and disc to align is compromised and in some cases even prevented as the binary separation shortens.

6.3 Bent trajectories and dual jets in a binary system

Jet precession is not the only interpretation for temporal changes in the apparent speed, position angle and flux density of jet components. Helical motions of the jet plasma can also produce bent trajectories on the plane of the sky (e.g., Steffen et al. 1995). Orbital motions in a SMBHB (e.g., Villata & Raiteri 1999), internally rotating jet flows (e.g., Camenzind & Krockenberger 1992), or even angular variations in the flow direction (e.g., associated with a precessing jet; Hardee 2000) are the usual mechanisms invoked in the literature to excite helical patterns in jets.

In the case of AO 0235+164, helical jet motions have also been proposed to explain either periodic variabilities in its continuum spectrum (Qian et al. 2000; Ostorero et al. 2004; Raiteri et al. 2006; Rani et al. 2009; Tripathi et al. 2021; Otero-Santos et al. 2023) or bent trajectories of jet components (Kutkin et al. 2018). Indeed, jet interactions with the external medium can also change the velocity of the jet components and/or deflecting them from their initial trajectories as they recede from the core, producing curved jet paths on the plane of the sky (e.g., Attridge et al. 1999; Homan et al. 2003; Lister 2008; An et al. 2020). Trailing compressions triggered by pinch-mode jet-body instabilities caused by the propagation of a strong perturbation (superluminal jet component) may also exhibit bent trajectories (e.g., Agudo et al. 2001; Gómez et al. 2001; Fromm et al. 2013).

Another scenario that could account for both the continuum variability and the kinematics of the parsec-scale jet components in AO 0235+164 involves dual jets produced by individual black holes in a binary system. Although, to the best of our knowledge, this possibility has not previously been suggested for AO 0235+164, it has been explored in other blazars (e.g., Qian et al. 2019, 2021), also offering a potential framework in which the collision of two relativistic parsec-scale jets might generate high-energy neutrinos (Britzen et al. 2019).

If this scenario applies to AO 0235+164, it is conceivable that some jet components identified in this study may be associated with a secondary black hole, rather than strictly following our precession models shown in Figure 5. In particular, the jet components C12–C19 (with apparent speeds of approximately $10c$ and position angles around -200°) are systematically below the curves predicted by our precession models in the $\beta_{\text{app}} - \eta$ plots, suggesting that these components might have been ejected by an active secondary black hole.

7 FINAL REMARKS

In this study, we analysed public radio interferometric maps of AO 0235+164 at 15 GHz and 43 GHz, obtained over nearly 30 years. They were modelled using two-dimensional elliptical Gaussian components, following the criteria of Caproni et al. (2014). The CE global optimization technique was applied to all 203 interferometric maps studied in this work (41 maps at 15 GHz and 162 maps at 43 GHz) and was used to estimate the structural parameters of these Gaussian components. Our main results are summarized as follows.

- We kinematically identified 36 parsec-scale jet components moving relativistically from the source's radio core. Their apparent velocities range from $3.0c$ to $34.3c$, and their mean position angles are distributed across all quadrants of the sky;

- Based on the kinematic of the jet components, we estimated the minimum jet bulk Lorentz factor to be 34.3 ± 6.6 and the maximum jet viewing angle to be $36.7 \pm 7.8^\circ$;

- The brightness temperature of the core region at 15 and 43 GHz ranges from about 7×10^{10} K to 2.2×10^{13} K, consistent with previous estimates and confirming that AO 0235+164 can reach $T_{B,\text{rest}}$ as high as 10^{13} K;

- Differences in the apparent velocity and position angle of the jet components suggest that the direction of the parsec-scale jet changes over time. An analytical precession model was used to simultaneously fit the right ascension and declination offsets, mean position angles, apparent velocities of the jet components, and the brightness temperature of the core region (for the first time in the literature);

- The seven free parameters of the jet precession model were determined using the CE global optimisation technique for both clockwise and counter-clockwise precession. The parameters γ , ϕ_0 and φ_0 obtained for both senses agree with each other within their respective uncertainties. The jet precession period at the observer's reference frame was found to be about 8.4 years for clockwise precession, slightly longer than the 6.0-year period for counter-clockwise precession. Both precession periods agree with some of the periodicities detected in the light curves of AO 0235+164;

- Both jet precession models fit the observational constraints fairly well, with clockwise precession being slightly favoured based on its merit function value (see Table 2). The coincidence between the main gamma-ray flares seen in the public *Fermi* light curve of AO 0235+164 and the peaks of the Doppler factor predicted by the clockwise jet precession provides an additional advantage over the counter-clockwise precession (see the bottom panels in Figure 5). However, as $S(k_{\text{max}})$ for clockwise and counter-clockwise precession differs by less than a factor of two, counter-clockwise precession cannot be completely ruled out for AO 0235+164;

- We investigated the possibility of the parsec-scale jet precession in AO 0235+164 is driven by a secondary SMBH in a non-coplanar circular orbit around a primary SMBH, assuming that its jet comes from the primary accretion disc torqued by the secondary SMBH. We found that the orbital period of the secondary must be roughly between 0.5 and 1 year for the ballistic precession or between 0.2 and 40 years in the non-ballistic scenario, which implies a separation between the primary and secondary black holes between 0.002 and 0.004 pc and 0.001 and 0.05 pc, respectively. Even though a so compact system cannot be angularly resolved by the current instrumentation, there is some room for gravitational wave experiments like Pulsar Timing Arrays (e.g., EPTA Collaboration et al. 2023) might detect such SMBHB in AO 0235+164;

- Katz et al. (1982) demonstrated that short-term oscillations (nodding motions) around the mean precession motion can occur in such SMBHB. For AO 0235+164 under a non-ballistic parsec-jet precession, the nodding period in the source's reference frame is roughly between 0.07 and 20 years, causing an amplitude oscillation around the precession motion of the disc between $0^\circ.003$ and $1^\circ.0$. Considering the later value, additional changes in the apparent velocities and position angles of the jet components between $-16c$ and $1.6c$ and -31° and 31° are respectively expected in this case. Indeed, a decrease of $16c$ in β_{obs} would be sufficient to reconcile our jet precession models with the jet components having $\eta \sim 200^\circ$ and $\beta_{\text{obs}} \sim 10c$ in the $\beta_{\text{obs}} - \eta$ plots shown in Figure 5;

- We also explore the possibility that the radio/optical periodic-

ities of 5-6 years and 2-3 years are respectively associated with the orbital period of the secondary SMBH and the jet's nodding motion, which better restricted the possible values of q_{BH} for the putative binary system in AO 0235+164. Thus, the SMBHB scenario explored in this work, along with the jet precession, can provide a physical interpretation for three periodicities found in the light curves of AO 0235+164;

- A SMBHB with the secondary SMBH orbiting the primary in a non-coplanar plane relative to the primary accretion disc is not the only physical mechanism that could induce disc/jet precession. In the case of geodetic precession (e.g., Barker & O'Connell 1975), a separation between the secondary and primary SMBHs must be smaller than about 3 mpc to make the parsec-scale jet of AO 0235+164 precesses at the rate inferred in this work for non-ballistic precession. A SMBHB like this is relatively stable in terms of gravitational wave losses ($\tau_{\text{GW},s} \sim 5251$ years). However, $d_{\text{BH}} \lesssim 7 \times 10^{-4}$ pc ($\tau_{\text{GW},s} \sim 13$ years) for the ballistic jet precession scenario, casting doubts on geodetic precession mechanism in this particular case;

- The Bardeen-Petterson effect (Bardeen & Petterson 1975) is a potential candidate for driving precession in misaligned accretion discs surrounding Kerr black holes. Considering the analytical formulae for the precession time-scale derived by Martin et al. (2009) for a steady-state disc with an outer radius much larger than the warping radius, we obtain precession periods longer than 10^6 years in the source's reference frame, incompatible with the precession periods found in this work for AO 0235+164. However, analytical work and numerical simulations show that the disc may break apart in some situations, with each segment precessing independently. The inner disc precesses at a faster rate, potentially explaining the precession of the jet in AO 0235+164. Indeed, the spin-induced precession (e.g. Liu & Melia 2002; Caproni et al. 2004) is able to recover the precession period inferred in this work if the outer radius of the inner disc is roughly smaller than some thousands of gravitational radius;

- Although the kinematic of the 36 jet components identified in this work is compatible with ballistic motions, nine of them present some scatter around their receding motions implied by the ballistic scenario. Helical motions of the jet plasma could be behind of those bent trajectories, which might be driven by the own jet precession (Hardee 2000), orbital motions in a SMBHB (e.g., Villata & Raiteri 1999), or in internally rotating jet flows (e.g., Camenzind & Krockenberger 1992);

- An alternative explanation for the variability and kinematics of AO 0235+164 involves dual relativistic jets produced by a binary black hole system. Though not previously proposed for this source, such scenarios have been invoked for other blazars (e.g., Qian et al. 2019, 2021). In this framework, jet components C12-C19 — exhibiting apparent velocities of $\sim 10c$ and position angles of about -200° — may originate from a secondary black hole, potentially deviating from the modelled jet precession curves. This interpretation could also imply conditions favourable for high-energy neutrino production via jet collisions (Britzen et al. 2019).

Although our jet precession models have captured the general trends of the kinematic of the parsec-scale jet of AO 0235+164, future studies, including high-cadence interferometric monitoring of the source's activity, are essential to confirm them, as well as the existence of a SMBHB in the nucleus of AO 0235+164.

ACKNOWLEDGEMENTS

F.B.S.J. thanks the Brazilian agency CAPES for financial support. We thank the anonymous referee for the constructive comments

and suggestions, which helped improve the original version of this manuscript. This research has made use of data from the MOJAVE database that is maintained by the MOJAVE team (Lister et al. 2018). This study makes use of 43 GHz VLBA data from the VLBA-BU Blazar Monitoring Program (VLBA-BU-BLAZAR; <http://www.bu.edu/blazars/VLBAproject.html>), funded by NASA through the Fermi Guest Investigator Program. The VLBA is an instrument of the National Radio Astronomy Observatory. The National Radio Astronomy Observatory is a facility of the National Science Foundation operated by Associated Universities, Inc.

DATA AVAILABILITY

The data generated in this research will be shared on reasonable request to the corresponding author.

REFERENCES

- Abdo A. A., et al., 2010, *ApJ*, **710**, 1271
- Abraham Z., 2000, *A&A*, **355**, 915
- Abraham Z., Romero G. E., 1999, *A&A*, **344**, 61
- Abraham R. G., Crawford C. S., Merrifield M. R., Hutchings J. B., McHardy I. M., 1993, *ApJ*, **415**, 101
- Agudo I., Gómez J.-L., Martí J.-M., Ibáñez J.-M., Marscher A. P., Alberdi A., Aloy M.-A., Hardee P. E., 2001, *ApJ*, **549**, L183
- Agudo I., et al., 2011, *ApJ*, **735**, L10
- Amaro-Seoane P., et al., 2017, *arXiv e-prints*, p. [arXiv:1702.00786](https://arxiv.org/abs/1702.00786)
- An T., et al., 2020, *Nature Communications*, **11**, 143
- Antonucci R., 1993, *ARA&A*, **31**, 473
- Attridge J. M., Roberts D. H., Wardle J. F. C., 1999, *ApJ*, **518**, L87
- Bardeen J. M., Petterson J. A., 1975, *ApJ*, **195**, L65
- Barker B. M., O’Connell R. F., 1975, *ApJ*, **199**, L25
- Bate M. R., Bonnell I. A., Clarke C. J., Lubow S. H., Ogilvie G. I., Pringle J. E., Tout C. A., 2000, *MNRAS*, **317**, 773
- Begelman M. C., Blandford R. D., Rees M. J., 1984, *Reviews of Modern Physics*, **56**, 255
- Blandford R., Meier D., Readhead A., 2019, *ARA&A*, **57**, 467
- Britzen S., et al., 2019, *A&A*, **630**, A103
- Bychkova V. S., et al., 2015, *Astronomy Reports*, **59**, 851
- Camenzind M., Krockenberger M., 1992, *A&A*, **255**, 59
- Caproni A., Abraham Z., 2004a, *MNRAS*, **349**, 1218
- Caproni A., Abraham Z., 2004b, *ApJ*, **602**, 625
- Caproni A., Mosquera Cuesta H. J., Abraham Z., 2004, *ApJ*, **616**, L99
- Caproni A., Livio M., Abraham Z., Mosquera Cuesta H. J., 2006, *ApJ*, **653**, 112
- Caproni A., Monteiro H., Abraham Z., 2009, *MNRAS*, **399**, 1415
- Caproni A., Abraham Z., Monteiro H., 2013, *MNRAS*, **428**, 280
- Caproni A., Melo I. T. e., Abraham Z., Monteiro H., Roland J., 2014, *MNRAS*, **441**, 187
- Caproni A., Abraham Z., Motter J. C., Monteiro H., 2017, *ApJ*, **851**, L39
- Chen Y. J., Zhang F. J., Sijouwerman L. O., 1999a, *New Astron. Rev.*, **43**, 707
- Chen Y. J., Zhang F. J., Sijouwerman L. O., 1999b, *Ap&SS*, **266**, 495
- Chen L., Wu S., Yuan F., 2009, *MNRAS*, **398**, 1900
- Cheong W. Y., et al., 2023, *Monthly Notices of the Royal Astronomical Society*, **527**, 882
- Chu H. S., Baath L. B., Rantakyroo F. T., Zhang F. J., Nicholson G., 1996, *A&A*, **307**, 15
- Cohen R. D., Smith H. E., Junkkarinen V. T., Burbidge E. M., 1987, *ApJ*, **318**, 577
- Cooper N. J., Lister M. L., Kochanzyk M. D., 2007, *ApJS*, **171**, 376
- Doğan S., Nixon C., King A., Price D. J., 2015, *MNRAS*, **449**, 1251
- Drewes N. C., Nixon C. J., 2021, *ApJ*, **922**, 243
- EPTA Collaboration et al., 2023, *A&A*, **678**, A48
- Escudero Pedrosa J., et al., 2024, *A&A*, **689**, A56
- Fan J.-h., Yang C. H., Gong H. M., 2000, *Chinese Astron. Astrophys.*, **24**, 1
- Fan J. H., Lin R. G., Xie G. Z., Zhang L., Mei D. C., Su C. Y., Peng Z. M., 2002, *A&A*, **381**, 1
- Fan J. H., et al., 2007a, in Ho L. C., Wang J. W., eds, *Astronomical Society of the Pacific Conference Series Vol. 373, The Central Engine of Active Galactic Nuclei*. p. 195
- Fan J. H., et al., 2007b, *A&A*, **462**, 547
- Fan J., et al., 2016a, *Galaxies*, **4**
- Fan J., et al., 2016b, *Galaxies*, **4**, 17
- Fan J. H., et al., 2017, *ApJ*, **837**, 45
- Frey S., et al., 2000, *PASJ*, **52**, 975
- Fromm C. M., et al., 2013, *A&A*, **551**, A32
- Gerosa D., Rosotti G., Barbieri R., 2020, *MNRAS*, **496**, 3060
- Gómez J.-L., Marscher A. P., Alberdi A., Jorstad S. G., Agudo I., 2001, *ApJ*, **561**, L161
- Hardee P. E., 2000, *ApJ*, **533**, 176
- Hayasaki K., Sohn B. W., Okazaki A. T., Jung T., Zhao G., Naito T., 2015, *J. Cosmology Astropart. Phys.*, **2015**, 005
- Homan D. C., Lister M. L., Kellermann K. I., Cohen M. H., Ros E., Zensus J. A., Kadler M., Vermeulen R. C., 2003, *ApJ*, **589**, L9
- Homan D. C., et al., 2006, *ApJ*, **642**, L115
- Homan D. C., Kadler M., Kellermann K. I., Kovalev Y. Y., Lister M. L., Ros E., Savolainen T., Zensus J. A., 2009, *ApJ*, **706**, 1253
- Homan D. C., et al., 2021, *ApJ*, **923**, 67
- Hovatta T., Valtaoja E., Tornikoski M., Lähteenmäki A., 2009, *A&A*, **494**, 527
- Hughes P. A., Aller H. D., Aller M. F., 1985, *ApJ*, **298**, 301
- Ivanov P. B., Illarionov A. F., 1997, *MNRAS*, **285**, 394
- Jones D. L., Baath L. B., Davis M. M., Unwin S. C., 1984, *ApJ*, **284**, 60
- Jorstad S. G., Marscher A. P., Mattox J. R., Aller M. F., Aller H. D., Wehrle A. E., Bloom S. D., 2001, *ApJ*, **556**, 738
- Jorstad S. G., et al., 2017, *ApJ*, **846**, 98
- Kaaz N., Liska M. T. P., Jacquemin-Ide J., Andalman Z. L., Musoke G., Tchekhovskoy A., Porth O., 2023, *ApJ*, **955**, 72
- Katz J. I., 1997, *ApJ*, **478**, 527
- Katz J. I., Anderson S. F., Margon B., Grandi S. A., 1982, *ApJ*, **260**, 780
- Kellermann K. I., Pauliny-Toth I. I. K., 1969, *ApJ*, **155**, L71
- King A. R., Lubow S. H., Ogilvie G. I., Pringle J. E., 2005, *MNRAS*, **363**, 49
- Konigl A., 1981, *ApJ*, **243**, 700
- Kovalev Y. Y., et al., 2005, *AJ*, **130**, 2473
- Kraus A., et al., 1999, *A&A*, **344**, 807
- Krause M. G. H., et al., 2019, *MNRAS*, **482**, 240
- Kumar S., Pringle J. E., 1985, *MNRAS*, **213**, 435
- Kutkin A. M., et al., 2018, *MNRAS*, **475**, 4994
- Larwood J. D., Nelson R. P., Papaloizou J. C. B., Terquem C., 1996, *MNRAS*, **282**, 597
- Lee S.-S., Lobanov A. P., Krichbaum T. P., Zensus J. A., 2016, *ApJ*, **826**, 135
- Lehto H. J., Valtonen M. J., 1996, *ApJ*, **460**, 207
- Lense J., Thirring H., 1918, *Physikalische Zeitschrift*, **19**, 156
- Liodakis I., Hovatta T., Huppenkothen D., Kiehlmann S., Max-Moerbeck W., Readhead A. C. S., 2018, *ApJ*, **866**, 137
- Liska M., Hesp C., Tchekhovskoy A., Ingram A., van der Klis M., Markoff S., 2018, *MNRAS*, **474**, L81
- Liska M., Hesp C., Tchekhovskoy A., Ingram A., van der Klis M., Markoff S. B., Van Moer M., 2021, *MNRAS*, **507**, 983
- Lister M. L., 2008, in Rector T. A., De Young D. S., eds, *Astronomical Society of the Pacific Conference Series Vol. 386, Extragalactic Jets: Theory and Observation from Radio to Gamma Ray*. p. 240 ([arXiv:0707.0474](https://arxiv.org/abs/0707.0474)), doi:10.48550/arXiv.0707.0474
- Lister M. L., et al., 2009, *AJ*, **138**, 1874
- Lister M. L., Aller M. F., Aller H. D., Hodge M. A., Homan D. C., Kovalev Y. Y., Pushkarev A. B., Savolainen T., 2018, *ApJS*, **234**, 12
- Liu S., Melia F., 2002, *ApJ*, **573**, L23
- Liu F. K., Zhao G., Wu X.-B., 2006, *ApJ*, **650**, 749
- Lobanov A. P., 2005, *arXiv e-prints*, [pp astro-ph/0503225](https://arxiv.org/abs/ppastro-ph/0503225)
- Lodato G., Price D. J., 2010, *MNRAS*, **405**, 1212
- Lodato G., Pringle J. E., 2006, *MNRAS*, **368**, 1196
- Lodato G., Pringle J. E., 2007, *MNRAS*, **381**, 1287
- Marscher A. P., Gear W. K., 1985, *ApJ*, **298**, 114

- Martin R. G., Pringle J. E., Tout C. A., 2009, *MNRAS*, **400**, 383
- Musoke G., Liska M., Porth O., van der Klis M., Ingram A., 2023, *MNRAS*, **518**, 1656
- Nandi S., Caproni A., Kharb P., Sebastian B., Roy R., 2021, *ApJ*, **908**, 178
- Nandi S., Kharb P., Caproni A., Roy R., Sebastian B., 2024, *ApJ*, **965**, 9
- Nealon R., Price D. J., Nixon C. J., 2015, *MNRAS*, **448**, 1526
- Nealon R., Ragusa E., Gerosa D., Rosotti G., Barbieri R., 2022, *MNRAS*, **509**, 5608
- Nelson R. P., Papaloizou J. C. B., 2000, *MNRAS*, **315**, 570
- Netzer H., 2015, *ARA&A*, **53**, 365
- Nixon C. J., King A. R., 2012, *MNRAS*, **421**, 1201
- Nixon C., King A., Price D., Frank J., 2012, *ApJ*, **757**, L24
- Nixon C., King A., Price D., 2013, *MNRAS*, **434**, 1946
- O’Dell S. L., et al., 1988, *ApJ*, **326**, 668
- Ogilvie G. I., 1999, *MNRAS*, **304**, 557
- Ogilvie G. I., 2000, *MNRAS*, **317**, 607
- Ostorero Villata, M., Raiteri, C. M. 2004, *A&A*, **419**, 913
- Otero-Santos J., Peñil P., Acosta-Pulido J. A., Becerra González J., Raiteri C. M., Carnerero M. I., Villata M., 2023, *MNRAS*, **518**, 5788
- Paliya V. S., Domínguez A., Ajello M., Olmo-García A., Hartmann D., 2021, *ApJS*, **253**, 46
- Peters P. C., Mathews J., 1963, *Physical Review*, **131**, 435
- Press W. H., Thorne K. S., 1972, *ARA&A*, **10**, 335
- Qian S. J., Kraus A., Witzel A., Krichbaum T. P., Zensus J. A., 2000, *A&A*, **357**, 84
- Qian S. J., Britzen S., Krichbaum T. P., Witzel A., 2019, *A&A*, **621**, A11
- Qian S. J., Britzen S., Krichbaum T. P., Witzel A., 2021, *A&A*, **653**, A7
- Raiteri C. M., et al., 2001, *A&A*, **377**, 396
- Raiteri C. M., et al., 2006, *A&A*, **459**, 731
- Raiteri C. M., et al., 2008, *A&A*, **480**, 339
- Raj A., Nixon C. J., Doğan S., 2021, *ApJ*, **909**, 81
- Rani B., Wiita P. J., Gupta A. C., 2009, *ApJ*, **696**, 2170
- Readhead A. C. S., 1994, *ApJ*, **426**, 51
- Rezzolla L., Yoshida S., Zanotti O., 2003, *MNRAS*, **344**, 978
- Rickett B. J., Lazio T. J. W., Ghigo F. D., 2006, *ApJS*, **165**, 439
- Rieger F. M., 2004, *ApJ*, **615**, L5
- Roland J., Britzen S., Caproni A., Fromm C., Glück C., Zensus A., 2013, *A&A*, **557**, A85
- Romero G. E., Chajet L., Abraham Z., Fan J. H., 2000, *A&A*, **360**, 57
- Romero G. E., Fan J.-H., Nuza S. E., 2003, *Chinese J. Astron. Astrophys.*, **3**, 513
- Roy M., Papadakis I. E., Ramos-Colón E., Sambruna R., Tsinganos K., Papamastorakis J., Kafatos M., 2000, *ApJ*, **545**, 758
- Roy A., et al., 2022, *MNRAS*, **513**, 5238
- Roy A., et al., 2023, *ApJS*, **265**, 14
- Rubinstein R. Y., 1997, *European Journal of Operational Research*, **99**, 89
- Rubio-Herrera E., Lee W. H., 2005, *MNRAS*, **357**, L31
- Scheuer P. A. G., Feiler R., 1996, *MNRAS*, **282**, 291
- Sebastian B., et al., 2024, *MNRAS*, **530**, 4902
- Shakura N. I., Sunyaev R. A., 1973, *A&A*, **24**, 337
- Shapiro S. L., Teukolsky S. A., 1983, *Black holes, white dwarfs, and neutron stars : the physics of compact objects*. John Wiley & Sons, Inc.
- Shepherd M. C., Pearson T. J., Taylor G. B., 1994, in *Bulletin of the American Astronomical Society*, pp 987–989
- Sillanpää A., Haarala S., Valtonen M. J., Sundelius B., Byrd G. G., 1988, *ApJ*, **325**, 628
- Smith A. G., Nair A. D., 1995, *PASP*, **107**, 863
- Steffen W., Zensus J. A., Krichbaum T. P., Witzel A., Qian S. J., 1995, *A&A*, **302**, 335
- Stickel M., Fried J. W., Kuehr H., 1988, *A&A*, **198**, L13
- Sumida V. Y. D., Schutzer A. d. A., Caproni A., Abraham Z., 2021, *MNRAS*, **509**, 1646
- Tremaine S., Davis S. W., 2014, *MNRAS*, **441**, 1408
- Tripathi A., Gupta A. C., Aller M. F., Wiita P. J., Bambi C., Aller H., Gu M., 2021, *MNRAS*, **501**, 5997
- Türler M., Courvoisier T. J. L., Paltani S., 2000, *A&A*, **361**, 850
- Ulrich M.-H., Maraschi L., Urry C. M., 1997, *ARA&A*, **35**, 445
- Urry C. M., Padovani P., 1995, *PASP*, **107**, 803
- Valtaoja E., Terasranta H., Urpo S., Nesterov N. S., Lainela M., Valtonen M., 1992, *A&A*, **254**, 71
- Villata M., Raiteri C. M., 1999, *A&A*, **347**, 30
- Vol’vach A. E., Larionov M. G., Vol’vach L. N., Lähteenmäki A., Tornikoski M., Aller M. F., Aller H. D., Sasada M., 2015a, *Astronomy Reports*, **59**, 145
- Vol’vach A. E., Larionov M. G., Vol’vach L. N., Lähteenmäki A., Tornikoski M., Aller M. F., Aller H. D., Sasada M., 2015b, *Astronomy Reports*, **59**, 145
- Volvach A. E., et al., 2019a, *Cosmic Research*, **57**, 85
- Volvach A. E., et al., 2019b, *Cosmic Research*, **57**, 85
- Wang H., 2014, *Ap&SS*, **351**, 281
- Wang Y.-F., Jiang Y.-G., 2020, *ApJ*, **902**, 41
- Wang H., Yin C., Xiang F., 2017, *Ap&SS*, **362**, 99
- Weaver Z. R., et al., 2022, *ApJS*, **260**, 12
- Webb J. R., Smith A. G., 1988, in Miller H. R., Wiita P. J., eds., , Vol. 307, *Active Galactic Nuclei*. Springer-Verlag, Berlin, New York, p. 176, doi:10.1007/3-540-19492-4_192
- Webb J. R., Howard E., Benítez E., Balonek T., McGrath E., Shrader C., Robson I., Jenkins P., 2000, *AJ*, **120**, 41
- Zhang F.-J., Chen Y.-J., Zhu H.-S., 1997, *Acta Astronomica Sinica*, **38**, 397

This paper has been typeset from a \LaTeX file prepared by the author.